THE EUROPEAN SOCIETY OF MEDICINE
Medical Research Archives, Volume 12 Issue 8

RESEARCH ARTICLE

Ferromagnetic carbon/graphite: from CBRN Defense to sensors applied to oncology as a promising way to detect and fight cancer and tumors/ neoplasms

Fernando M. Araujo-Moreira*[1]

[1] Military Institute of Engineering/IME, Department of Science and Technology, Brazilian Army; Nuclear Engineering Graduate Program (PPGEN); Praça General Tibúrcio 80, Urca, Rio de Janeiro RJ, 22290-270, Brazil

*fernando.manuel@ime.eb.br

OPEN ACCESS

PUBLISHED
31 August 2024

CITATION
Araujo-Moreira, F.M., 2024. Ferromagnetic carbon/graphite: from CBRN Defense to sensors applied to oncology as a promising way to detect and fight cancer and tumors/neoplasms. Medical Research Archives, [online] 12(8). https://doi.org/10.18103/mra.v12i8.5508

DOI
https://doi.org/10.18103/mra.v12i8.5508

ISSN
2375-1924

ABSTRACT

The emerging field of multifunctional sensors for different application sectors requires high sensitivity, accuracy, reproducibility, mechanical flexibility, and low cost for a wide range of applications, from medicine to security and defense. While many national defense institutions and services have developed sensors to detect chemical, biological, radiological and nuclear threats (i.e., for CBRN Defense), better sensors are needed as well as the ability to feed the right data quickly into command centers for analysis and action on threats. All these new devices depend on new material like the so-called nanocarbons, with novel properties and morphologies. For example, nanocarbons, such as graphene, are beginning to be obtained from the use of pulsed laser deposition (PLD) to manufacture sensors for the detection of substances that can be used as chemical warfare agents. On the other side of novel applications, nanostructured materials are beginning to be used in nanomedicine. This is the case of nanostructured carbon used as a drug carrier. This is the main subject of the present article. Despite all the incredible and recent advances in all technological areas, including those applied to medicine, depending on the stage of detection, cancer is still a difficult-to-treat disease associated with a negative prognosis. Each year, the American Cancer Society estimates the number of new cancer cases and deaths in the United States and compiles the most recent data on population-based cancer occurrence and outcomes. As expected, it shows that cancer is one of the leading causes of death, accounting for millions of deaths worldwide each year. All over the last decade, new techniques and methods for the prevention, diagnosis, and treatment of diseases based on new materials and new morphologies have emerged. Many of the basic technologies of medical physics are well-established, using well-understood physics principles. Clinical applications of those technologies have improved spectacularly, in many cases because of improvements in physics and engineering. In this context, new materials have been playing an important role. Carbon is starting to be one of those materials with promising applications in medicine, especially ferromagnetic carbon/graphite. The occurrence of magnetism in carbon-based materials has been the subject of many investigations and some controversy over the past four decades, given the enormous interest in the possibility of producing carbon-based magnetic materials free from metallic elements like Fe, Co, and Ni. Exactly two decades ago, in 2004, we presented to the scientific community a very low-cost chemical route to reach one of the most sought-after materials in the history of science: pure organic carbon-based magnetic material stable at room temperature. The prospect of carbon-based magnetic materials like that, has been of immense fundamental and practical importance. Information on atomic-scale features was required for a better understanding of the mechanisms leading to carbon magnetism. That came out only in 2015, when we published an article at *Nature Scientific Reports*, reporting strong and incontrovertible results proving that magnetism in this material was genuine and independent of the presence of any magnetic impurity. We presented experimental confirmation that its magnetism originates from defects in the atomic structure. Those results were obtained from direct measurement of the local magnetic field using ^{13}C nuclear magnetic resonance associated with the numerical results obtained from DFT (Density-Functional Theory) calculations. In this review, exclusively about our own work, we describe the obtention and main properties of carbon-based nanostructured magnetic material and how it is starting to be one of those materials with promising applications in medicine.

Here, we give a comprehensive and complete view of our search looking for the obtention of this material, which is stable at room temperature and is free from metallic ferromagnetic elements. Besides its chemical obtention and properties, here we show its use from magnetic bio-hybrid matrices until the so-called MAGUS® (**MA**gnetic **G**raphite **U**niversal **S**ystem), a sensor with promising applications in oncology aiming to detect and fight cancer and tumors/neoplasms.

The paper is organized as follows: (a) in section 1 we give the scope and purpose of the article; (b) in section 2 we describe the discovery, the intrinsic nature, the nanofluid behavior, and the potential for both a drug delivery system and the use for diagnosis or imaging of carbon-based nanostructured magnetic material; (c) in section 3 we show the detailed methodology and explanation of why the methods were chosen following the same order of those topics of section 2; (d) in section 4 we show and discuss the obtained results and we answer all research open questions; and (e) in section 5 we give the conclusions. At the end, we give a list of references, most of which are our own.

Keywords: Carbon-based magnetic materials; carbon/graphite; nanofluid ferromagnetic carbon; ferromagnetic carbon; drug carriers; magnetic particle imaging.

1. Introduction

Throughout history, countless technological advances, originally intended for the development of military products and systems, have spilled over to other sectors, generating disruptive innovations with enormous benefits for society[1,2]. Particularly in the twentieth century, sophisticated research of military interest boosted innovations and the economic growth of pioneering countries. Today, the so-called fourth industrial revolution is transforming the way people relate, work and enjoy their leisure and rest hours. On a broader spectrum, it is affecting economic growth, development, security and sovereignty of countries, international relations and the nature of warlike conflicts among other areas. Unlike its predecessors, which are based on disruptive innovations in specific areas, the fourth industrial revolution develops from the confluence of innovations that have occurred in various areas. Physics comprises incessant and surprising advances in new materials, sensors, nanotechnology, microelectronics and the physical infrastructure of information and communication technologies; communication protocols, and algorithms used in a wide range of applications. Genetic algorithms, artificial neural networks, learning techniques, genetic sequencing and bioprinting are some of the lines of research inspired by such studies.

Especially in the previously mentioned military system, the emerging field of multifunctional sensors for different military applications requires high sensitivity, accuracy, reproducibility, mechanical flexibility and low cost. The ability to empower robots and future electronic skin (e-skin) with high resolution, high sensitivity, and rapid response sensing capabilities is of interest to a broad range of applications. Those include wearable healthcare devices, biomedical prosthesis, and human–machine interacting robots such as service robots for the elderly and electronic skin to provide a range of diagnostic and monitoring capabilities, among others. While many national defense institutions and services have developed sensors to detect chemical, biological, radiological and nuclear threats (i.e., for CBRN Defense), better sensors are needed as well as the ability to feed the right data quickly into command centers for analysis and action on threats. All these new devices depend on new material like the so-called nanocarbons, with novel properties and morphologies. For example, nanocarbons, such as graphene, are beginning to be obtained from the use of pulsed laser deposition (PLD) to manufacture sensors for the detection of substances that can be used as chemical warfare agents.

On the other side of novel applications, nanostructured materials are beginning to be used in nanomedicine, the medical application of nanotechnology. This area ranges from the medical applications of nanomaterials and biological devices to nanoelectronic biosensors and molecular nanotechnology such as biological machines. Functionalities can be added to nanomaterials by interfacing them with biological molecules or structures. The integration of nanomaterials with biology has led to the development of diagnostic devices, contrast agents, analytical tools, physical therapy applications, and drug delivery systems. This is the case of nanostructured carbon described in this work as a drug carrier proposed as a promising way to detect and fight cancer and tumors/neoplasms, main subject of this article.

Despite all the recent technological advances, cancer is still a difficult-to-treat disease associated with a negative prognosis (depending on the stage of detection) that kills millions of people a year worldwide. Each year, the American Cancer Society estimates the number of new cancer cases and deaths in the United States and compiles the most recent data on population-based cancer occurrence and outcomes. The most common cancers are breast, lung, colon, rectum, and prostate cancers[2].

It was a leading cause of decease, accounting for nearly 10 million deaths in 2020, or nearly one in six deaths. In 2022, 1,918,030 new cancer cases and 609,360 cancer deaths were projected to occur just in the United States, including approximately 350 deaths per day from lung cancer, the leading cause of cancer death. In 2024, the number of cancer cases is expected to increase to 2,001,140 and 611,720 cancer deaths are projected to occur in the United States. Cancer mortality continued to decline through 2021, averting over 4 million deaths since 1991 because of reductions in smoking, earlier detection for some cancers, and improved treatment options in both adjuvant and metastatic settings[2]. Even today, most methods to treat that disease are based on surgery, chemotherapy, radiation therapy, or bone marrow transplantation. In many cases, it is necessary to combine more than one modality. However, some of those methods result in broad unwanted side effects because they have no specificity and reach not only cancer but other parts of the human body. Unquestionably, all methods have saved hundreds of thousands of lives, however, cancer is still killing too many people worldwide. It is highly desirable to develop new and more effective methods to specifically fight it.

In 2004, we reported (and patented) by the first time on a simple chemical route aiming to synthetize stable room-temperature magnetic bulk carbon. We obtained the experimental confirmation that its magnetism originates from defects in the structure (and not from ferromagnetic impurities like Fe, Ni or Co). This was obtained from direct measurement of the local magnetic field using ^{13}C nuclear magnetic resonance associated to the numerical results obtained from DFT (*Density-Functional Theory*) calculations. We have also developed the chemical synthesis route to obtain nanofluid ferromagnetic carbon/graphite.

In this short review exclusively about our own work, we briefly show these findings as well as the main physical and chemical properties of this material and recent results aiming biotechnological and medical applications. From theoretical calculation, we have analyzed its possible use as a contrast, for example, in the MPI (Magnetic Particle Imaging) technique. Finally, we show here the potential of this material to be used as a drug carrier to reach different targets like those associated with cancer, diabetes and Alzheimer by using what we have called MAGUS® (***MA****gnetic* ***G****raphite* ***U****niversal* ***S****ystem*).

2. Scientific Background

In this section, we describe the discovery, the intrinsic nature, the nanofluid behavior, and the potential for both

a drug delivery system and the use for the diagnosis of carbon-based nanostructured magnetic material. Here, together with the content of the next sections, we provide adequate scientific support for all claims based on our own references.

2.1 THE DISCOVERY OF FERROMAGNETIC CARBON/ GRAPHITE[3,4].

Over the last *few* years, the survey for macroscopic magnetic ordering phenomena in organic materials has been one of the most exciting and interesting subjects in science. Nanostructured carbon materials have increasingly attracted the interest of the scientific community, not only because of their physical properties but mainly because of their potential applications in high-tech devices. The possibility of achieving striking properties in macroscopic carbon—such as room-temperature magnetic properties and even superconductivity—open up a plethora of possible and striking applications. To cite just a few of them, these carbon-based materials could be used in nanotechnology, sensors, detectors, actuators, among others, for applications in medicine—magnetic imaging—or even applications in telecommunications, electronics, biosensors, magnetic materials separation, etc. For these reasons, obtaining macroscopic quantities of bulk room-temperature ferromagnetic carbon like carbon would be of fundamental and general interest, not only for a wide number of natural sciences, but mainly for technological applications of this material in engineering, as well as in medicine and biology, as a biocompatible magnetic material. The existence of pure carbon materials exhibiting ferromagnetic properties has hardly been believed to be true for many years. However, more than 100 articles, and about 30 patents, have been reported for ferromagnetic carbon-based materials consisting only of carbon or including elements of the first rows of the periodic table such as B, N, and S. Recent reports indicate that the ferromagnetic phase in those materials originates in the form of magnetic islands in a nonmagnetic matrix. In the last few years, this field of research has been renewed after the discovery of allotropic forms of carbon, p*articularly* after the discovery of ferromagnetism in the charge-transfer salt [TDAE]+C60and in polymerized fullerenes. Also, some other reports have proved the existence of weak ferromagnetic-like magnetization loops in highly oriented pyrolytic carbon (HOPG). C*onversely*, experiments performed on extraterrestrial carbon obtained from a meteorite have pointed to the presence of ferromagnetic carbon. In this case, the total experimental magnetization exceeded the calculated magnetization by a factor of 1.5 which had been attributed to ferromagnetic carbon, which constituted more than half of the meteorite mass. To demonstrate that the existence of ferromagnetism in pure carbon is unambiguously possible, very recently there have been reported two remarkable papers. In the first one, Esquinazi et al. report the induction of magnetic ordering by proton irradiation performed on HOPG samples. After the irradiation, the material exhibits stable magnetic ordering at room temperature. In the second paper, Rode et al. report the synthesis of an allotropic form of carbon—an all-carbon nanofoam—that exhibits ferromagnetic-like behavior up to 90K, with a narrow hysteresis curve and a high saturation magnetization. In this paper, we report on the magnetic properties of pure bulk ferromagnetic carbon/graphite, obtained by a chemical route we have recently reported. This method consists of a controlled etching on the carbon structure by a vapor phase redox reaction in a closed nitrogen atmosphere with copper oxide. This modified carbon has a strong magnetic response even at room temperature, where it can be attracted by any commercial magnet. Several samples have been prepared and all of them exhibited stable magnetic behavior. The first one, prepared in 2004, is still magnetic even after two decades.

2.2 CORROBORATING THE INTRINSIC NATURE OF CARBON MAGNETISM: DFT CALCULATIONS AND NMR EXPERIMENTS[5].

The occurrence of magnetism in carbon materials has been the subject of many investigations and some controversy over the past two decades, given the enormous interest in the possibility of producing carbon-based magnetic materials free from metallic elements. These biocompatible magnetic materials find applications in fields such as drug delivery and magnetic resonance imaging, among others. Moreover, the design of graphene-based spintronics devices would greatly benefit from a deeper understanding of magnetism and hyperfine interactions in carbon materials. Recent experimental evidence of magnetic properties (with reports of ferromagnetic order in some cases) of carbon-based materials include irradiated carbon, nanocarbons, fullerenes, oxygen-containing carbons and point defects in graphene. From the theoretical point of view, magnetism in graphene and related materials has been universally associated with the occurrence of defects such as atomic vacancies, chemisorbed species (such as fluorine, hydrogen and oxygen) and edge sites. Similar examples of defect-induced magnetism have also been reported in other materials free from transition metal or rare earth elements, such as organic magnets, oxides, nitrides, silicon carbide and others; in all these cases, a common point is the source of magnetism being related to the spin polarization of p orbitals, which is associated with the occurrence of defects of structural or chemical origin. Despite this, there is still some skepticism about the possibility of intrinsic magnetic effects in carbon-based materials, due to the ubiquitously questioned presence of minor amounts of iron or other metallic impurities in experimentally produced samples that could be the actual source of magnetism. However, there are several recent examples of careful analyses that demonstrate convincingly the intrinsic nature of magnetism in carbon-derived materials. X-ray magnetic circular dichroism (XMCD) is an element-specific technique that allows the assessment of information about the magnetic moments associated with different elements in the material. XMCD data obtained at the carbon K edge have shown that the magnetization of proton-irradiated samples of carbon films and carbon (as well as for virgin carbon) is indeed associated with the spin polarization of carbon π electrons and also with chemisorbed hydrogen. Similar results were achieved for ion irradiated SiC crystals, where the ferromagnetic properties of the material were ascribed to electrons in p orbitals of atoms in the neighborhood of atomic vacancies. On the other hand, the use of particle-induced x-ray emission has allowed the determination of elemental contents of common magnetic metals (such as Fe, Ni, Cr, etc.) down to sub-ppm

levels in samples of carbon and other carbon materials. With this detailed knowledge about the amounts of impurities, it is now possible to ascertain in many well-documented cases of carbon materials that, even when present, the impurities cannot account alone for the magnetization values and also cannot explain the temperature dependence of the magnetic properties of the analyzed materials. If intrinsic magnetism is indeed a feature of carbon-based materials, then the influence of the local magnetic field on carbon nuclei should be detectable – in the case of systems possessing magnetic order, a strong microscopic field termed the hyperfine field (B_{hf}) at the atomic nuclei is anticipated. Therefore, evidence for B_{hf} and measurements of its properties are highly desirable for a better understanding of magnetism in carbon-based materials, providing information on the source of magnetism from a local perspective. Besides its importance from a fundamental point of view, the hyperfine interactions are relevant for applications of graphene and related materials in spintronics and quantum information processing, leading to numerous theoretical calculations and experimental investigations involving the use of different techniques – electron spin resonance (ESR), muon spin rotation (μSR) and perturbed angular distribution. In none of these reports, however, any clue about the B_{hf} value in a truly ferromagnetic carbon material was ever reported. Here we presented a direct measurement of the local magnetic field using ^{13}C nuclear magnetic resonance (NMR), corroborating the intrinsic nature of magnetism in carbon and comparing the results to DFT calculations, confirming that the magnetism originates from defects in the structure, and not from ferromagnetic impurities.

2.3 MAKING POSSIBLE BIOTECHNOLOGICAL APPLICATIONS: FERROMAGNETIC CARBON/GRAPHITE AS A NANOFLUID[6,7].

Nanofluids can be defined as fluids containing suspended solid particles with sizes on the nanometers scale. In recent years, substantial progress has been made in developing technologies in the field of magnetic microspheres, nanospheres and nanofluids. A most recognizable class of magnetically controllable nanofluids (simultaneously exhibiting both fluid and magnetic properties) are suspended colloids of nano sized iron oxide particles (Fe_3O_4 or g-Fe_2O_3). At the same time, biocompatible ferrofluids normally use water as a vehicle. To prevent agglomeration, the magnetic nanoparticles have to be stabilized by ionic interaction using some kind of bioagent (like fatty, aspartic and glutamic acids or peptides). Alternatively, the co-precipitation of ferrous/ferric ions can be performed in the presence of the appropriate biopolymer (such as polyvinyl alcohol or polyethylene glycol). Several clinically important enzymes and proteins (including, among others, bovine serum albumin, streptokinase, chymotrypsin, and glucose oxidase) have been immobilized based on this method. On the other hand, carbon materials constitute one of the most fascinating classes of structures, exhibiting a wide variety of forms and properties. They have been increasingly attracting the attention of the scientific community mainly because of their potential applications in high-tech devices. For these reasons, the availability of macroscopic quantities of bulk room-temperature magnetic carbon-like is of utter importance not only for a wide number of natural sciences, but also for technological applications of this material in engineering (as well as in medicine and biology). We have already reported the method to obtain macroscopic quantities of pure bulk ferromagnetic carbon/graphite. The as-obtained modified carbon has a strong magnetic response even at room temperature (which manifests itself through a visible attraction by a commercial magnet).

Here, we briefly present the chemical route for synthesizing as well as its structural and magnetic properties. We emphasize that MG constitutes a unique material at the nanoscale level which is both magnetic and 100% organic. Both characteristics together give an enormous plethora of potential uses, ranging from applications in biomedicine (such as imaging, magnetic drug targeting and delivering, hyperthermia, etc.) to applications in paints and inks.

2.4 BIONANOCOMPOSITES AND FERROMAGNETIC CARBON/GRAPHITE: POTENTIAL SYSTEM FOR DRUG DELIVERY[8].

Nowadays, numerous studies are focused on the development of bio-hybrid systems, including those denoted as bionanocomposites that are based on biopolymers and nanoparticulated inorganic solids, **to** exploit their properties for an extensive range of applications. These kinds of materials are especially interesting in the biomedical field thanks to their safety and biocompatibility, being applied from wound dressing and tissue engineering to drug delivery. The advance in the drug delivery systems (DDS) based on bionanocomposite materials provides materials with efficient chemical or physical barriers to control the speed of the drug release and the maintenance of the desired dose, combined with a simple, cheap, versatile and biocompatible synthesis process. The biocompatible character of biopolymers such as polysaccharides or proteins has been widely profited for application in the controlled release of drugs. Among the polysaccharide group, alginate is commonly used in the development of DDS. It is a linear polysaccharide comprised of a-L-guluronic acid and b-D-mannuronic acid, which is extracted from brown seaweeds. It can be easily processed as beads, films, or foams for dissimilar applications. Alginate presents an advantageous property, as it can form a gel by crosslinking reactions with divalent cations, such as Ca^{2+} and Zn^{2+}, decreasing its solubility and often improving other properties such as mechanical resistance. These types of reactions are very useful in the preparation of beads as well as in the stabilization of films or foams for more diverse applications. Alginate-based bionanocomposites applied as DDS usually incorporate a hybrid material prepared by previous intercalation of the drug in a layered substrate such as clays and double hydroxides (LDH), to increase the stability of the system to procure an increased control over the release of the entrapped drug. Layered double hydroxides (LDHs) consisting of brucite-like layers composed of hydroxides of divalent and trivalent metal cations are commonly used as the inorganic counterpart of bio-hybrid systems for DDS purposes, due to their large anion exchange capacity and biocompatibility. Besides a wide variety of drugs, several types of biomolecules have been intercalated

into the brucite-like layers of LDHs, such as the anticoagulant heparin, phenylalanine and other amino acids or even DNA. Exclusive properties can be achieved by incorporating magnetic nanoparticles into the biopolymer matrices. Actually, a large number of magnetic materials have been used for abundant technological and biomedical applications, including magnetic separation, MRI contrast agents, hyperthermia, thermal ablation and tissue engineering. For the DDS area, this is one of the most interesting purposes, especially for cancer therapy, where the levels of drug release can be tuned through stimulation by an external magnetic field. In this context, LDH-drug containing materials provided with magnetic properties typically containing iron-oxide particles are currently explored in view of DDS applications. The incorporation of magnetic properties to LDH-based DDS can be used to procure a targeted controlled delivery of the drug as recently pointed out by Huang et al. The major drawback of many of the abovementioned magnetic DDS is related to the use of toxic reagents (e.g., organic solvents, initiators, or surfactants), frequently required in the synthesis process or in the preparation of the nanoparticle's dispersion, as they are undesirable for biomedical applications. In this sense, novel MG nanoparticles patented by our research groups were produced by a cheap and simple process based on the oxidation-reduction reaction of pristine carbon with controlled amounts of oxygen released from the decomposition of CuO at high temperatures, allowing to obtain macroscopic amounts of magnetic pure carbon nanoparticles. These nanoparticles synthesized according to predetermined parameters can be easily dispersed in bidistilled water only by sonication, in the absence of the usually required surfactants, organic solvents, or initiators. Thus, this carbonaceous material may be potentially used in a broad range of applications, especially for biomedical purposes such as tissue engineering, hyperthermia and DDS.

Here, we show the development of magnetic biohybrid matrices based on the combination of alginate and MG nanoparticles, in which the nonsteroidal anti-inflammatory drug ibuprofen (IBU) alone or intercalated in an Mg-Al layered double hydroxide (LDH) was chosen as the third component of the new type of magnetic bionanocomposite DDS. It is expected that the system involving the biopolymer and the two inorganic solids will combine three main advantages: (i) the protection afforded by the biocompatible alginate and its ability to be prepared as beads and films, (ii) the presence of MG nanoparticles that improve the physical and mechanical properties of the biopolymer and afford hydrophobic and magnetic character, and (iii) the protective effect of the LDH layers entrapping the IBU molecules that slow down the release rate of the drug. To confirm these assumptions, in vitro tests were carried out to evaluate the behavior of these new magnetic bionanocomposite materials in the controlled delivery of the entrapped ibuprofen.

2.5 THE FUTURE IN DIAGNOSIS: MAGNETIC PARTICLE IMAGING TECHNIQUE (MPI)[9].

The members of the class of materials called *magnetic* can be classified by their magnetization and/or their magnetic susceptibility to an applied magnetic field into diamagnetic, paramagnetic, and ferromagnetic materials. Superparamagnetism is a form of magnetism that appears in ferromagnetic nanoparticles, among other types of magnetic materials. If those nanoparticles are sufficiently small, the magnetization can randomly flip its direction under the influence of temperature. The magnetization curve of the assembly as a function of the applied magnetic field is a reversible S-shaped curve. Potential nano-systems for **use** in biological and medical applications are the so-called nanofluids defined as fluids containing suspended solid nanoparticles of different sizes. A most recognizable class of magnetically controllable nanofluid simultaneously exhibiting both fluid and magnetic properties is the ferrofluid, a suspended colloidal fluid of nanosized iron oxide (Fe_3O_4 or g-Fe_2O_3) particles frequently called SPIO. When used in MPI, the nanoparticles are sufficiently small and the ferrofluid suspension becomes superparamagnetic. Instead of ferrofluids, a new nanofluid based on pure ferromagnetic carbon/graphite is investigated as **a** contrast material for MPI in this paper. Carbon materials, especially nanocarbons, constitute one of the most fascinating classes of structures, exhibiting a wide variety of forms and properties. The possibility of achieving striking properties in macroscopic carbon - such as room-temperature magnetic properties and even superconductivity – is attracting the scientific community and opening up a plethora of possible applications of this material in engineering, as well as in medicine and biology, as a biocompatible magnetic material. While the basic research of ferromagnetic carbon/graphite is in progress, a model describing ferromagnetic magnetization is already available. This allows studying the suitability of ferromagnetic materials, e.g. nanofluid ferromagnetic carbon/graphite, in MPI.

3.Experimental Methods.

In this section, we describe in sufficient detail every experimental method related to (a) the synthesis and characterization of stable room temperature bulk MG samples; (b) the intrinsic nature, (c) the nanofluid behavior, (d) the potential for building a drug delivery system and (c) the potential use for imaging diagnosis of carbon-based nanostructured magnetic material. All figures obtained from those experiments are presented, analyzed and discussed in section 4, *Results and Discussions*.

3.1 SYNTHESIS AND CHARACTERIZATION OF STABLE ROOM TEMPERATURE BULK FERROMAGNETIC CARBON/GRAPHITE[3,4].

The chemically modified carbon described here was produced by a vapor phase redox reaction in **a** closed nitrogen atmosphere (N_2, 1 atm.) with copper oxide (CuO). A few grams of both powders, CuO (Merck, analytical grade) and carbon (Fluka, CAS number 7782-42-5, lot 426277/1, granularity < 0.1mm) were placed at different alumina crucibles in a sealed atmosphere, inside a tube furnace — typically 12 g of CuO and 3 g of carbon. The reaction vessel was an alumina tube. The reaction took place at 1200ºC, for 24 h. After the reaction completed, the CuO was partially reduced to Cu(0) and, in the other container, the carbon material showed a decrease in volume a 25% to 50% decrease in weight, especially in the side closest to the CuO crucible. Two different regions could be observed: (a) an upper layer, black and opaque, with an amorphous

aspect; (b) a lower layer, more crystalline than the original pure carbon. The material from the upper layer was the one that exhibited the magnetic behavior, detectable up to room temperature. The separation of both materials was carefully achieved with the aid of a magnet. The reproducibility of the method and purity of the materials, with special concern on the presence of metallic impurities, was regarded. Several samples have been prepared and all exhibited the magnetic behavior described here. Since the presence of any kind of ferromagnetic impurity must be avoided, we have carefully determined the chemical purity of the samples with atomic absorption spectroscopy (AAS) using a Shimadzu AA6800 spectrometer and checked these results with x-ray fluorescence analysis (XRF) and energy dispersive spectroscopy (EDS), comparing the results obtained for the pristine and the modified carbon. We have also studied the obtained MG samples by x-ray diffraction and scanning electron microscopy (SEM). These studies were performed using a Seifert Scintag PAD-II powder diffractometer, with CuKa radiation (1.5418 Å) and a Jeol JSM 5900LV microscope, respectively. We have magnetically characterized our treated carbon samples by performing magnetic measurements using a MPMS-5T Quantum Design magnetometer.

3.2 DFT CALCULATIONS AND NMR EXPERIMENTS[5].

(a) Samples.

The samples of powder ferromagnetic carbon/graphite were obtained by a chemical route consisting of a controlled etching on the synthetic carbon structure by a vapor phase redox reaction in a closed argon atmosphere (Ar, 1 atm.) with copper oxide (CuO). The chemical, structural and magnetic properties of all analyzed samples of ferromagnetic carbon/graphite were verified by different techniques, including atomic absorption spectroscopy (AAS), x-ray fluorescence analysis, energy dispersive spectroscopy, x-ray diffraction, scanning electron microscopy, atomic and magnetic force microscopy, and SQUID magnetization measurements as a function of absolute temperature and applied magnetic field. The average metal concentrations determined by AAS for samples prepared using the same experimental method in different batches are (in weight ratios): Fe – 64ppm; Co – 0.2ppm; Ni – 1.2ppm; Cu – 3.5ppm; Zn – 1.0ppm. As mentioned above, these values are too small to account for the sample saturation magnetization observed at low temperature. For example, in the most unfavorable situation (from the point of view of impurity-originated magnetism), all Fe content would be associated with ferromagnetic metallic Fe aggregates or Fe_3O_4 particles (which is quite unlikely). Even in this case, the Fe content in this sample would lead to a saturation magnetization at low temperatures around 0.01 or 0.006 emu/g, respectively. These values are orders of magnitude below the observed saturation magnetization. It is thus clear that the magnetic properties of ferromagnetic carbon/graphite are not due to impurities, similar to what has been reported for other types of magnetic carbons.

(b) DFT calculations.

The five systems shown in Fig. 1 were investigated using DFT. In the case of system E, the 3-dimensional structure of the carbon nanoribbon was generated by using periodic boundary conditions along the direction perpendicular to the layers. A full structural optimization of all studied systems was performed. For the exchange correlation potential, the generalized-gradient approximation (GGA) in the Perdew-Burke-Ernzerhof (PBE) scheme was used, as implemented in the VASP code. The lattice parameter for graphene obtained from structural optimization was 2.46Å. All calculations were carried out with spin-polarization and with a plane-wave-cutoff energy of 400 eV; the Brillouin zone integration was performed using the Monkhorst-Pack scheme with a 5× 5× 1 k-point mesh. The lattice parameter was kept fixed at the calculated value, whereas the atoms were allowed to relax until the atomic forces were smaller than 0.025 eV/Å. From the relaxed atomic structure of the studied systems, further DFT calculations were conducted to determine the hyperfine magnetic fields, using the all-electron full-potential linearized augmented plane-wave plus local-orbital method as implemented in the WIEN2k package. The muffin-tin radii for carbon and oxygen atoms were selected as RMT= 1.25. The cutoff wavevector RMTKMAX was taken to be 7.0. Self-consistency of the calculations was achieved with energy and charge convergence criteria set to 0.01 mRy and 0.0001 e, respectively.

(c) NMR experiments.

NMR experiments were performed using a Tecmag Apollo pulsed NMR spectrometer and an Oxford Instruments high-homogeneity variable field superconducting magnet with a helium variable temperature insert. NMR spectra were acquired with a conventional Hahn echo pulse sequence, $\pi/2$-τ-π-echo with a constant echo delay of either 13µs or 5µs (for measurements above 1.5K). The length of the 'optimal' $\pi/2$ pulse was found to be ambiguous due to RF enhancement effects, so a fixed pulse length of 0.5µs was chosen for all experiments. The sample and the NMR coil were immersed in a liquid-gas helium cryostat at atmospheric pressure.

3.3 FERROMAGNETIC CARBON/GRAPHITE AS A NANOFLUID[6,7].

The chemically modified ferromagnetic carbon/graphite described here was produced by a vapor phase redox reaction in closed nitrogen atmosphere (N_2, 1 atm.) with copper oxide using synthetic carbon powder (Fluka, granularity <0.1 mm). After obtaining the ferromagnetic carbon/graphite, we prepared the ferromagnetic carbon/graphite nanofluid suspension by dissolving carbon in acetone, adding a Cetyltrimethylammonium bromide (CTAB) cationic surfactant, and bringing it to an ultra-sonic edge. The resulting homogeneous solution was separated in a centrifuge at 6000 rpm. After five consecutive washes with acetone (to remove an excessive surfactant), deionized water was added, and the solid sample was brought back to an ultra-sonic edge for 1 min. The above procedure provided the necessary homogeneity and stability of the obtained solution. The adsorption of active agents on the surface of the carbon results from the favorable interaction between the surface and species of the solid adsorbents. Various interactions (such as electrostatic attraction, covalent binding, hydrogen binding, non-polar interactions, and lateral interactions between adsorbed species) can contribute to the adsorption processes, facilitating the aqueous suspension of carbon. Recently, this field of

research has been renewed by studies with fluid carbon nanotubes, among other forms. To assess the presence of CTAB molecules on the surface of nanofluid ferromagnetic carbon/graphite, we performed the micro-Raman analysis with samples of carbon dried in a vacuum at a temperature of 60°C for 6h.

The results revealed the presence of the peak at 1650 cm^{-1} corresponding to nanofluid ferromagnetic carbon/ graphite, in addition to the peak at 1350 cm^{-1}(known as the "disordered" D band) in the magnetic carbon/ graphite sample. For further comparison, the result also depicts the Raman spectrum showing characteristic bands of the surfactant used in the suspension (CTAB). Observe that, as expected, the CTAB functional groups, the hydrophobic (carbonic chain) and hydrophilic (cationic-active tensions with positive charge) parts of the surfactant correlate with the band structure of the carbon. Since the hydrophilic part tends to bind with the water molecules, its action results in the stabilization of the nanofluid suspension. The structural characterization of nanofluid ferromagnetic carbon/ graphite was performed by transmission electron microscopy (TEM) using the Philips CM-120 microscope. TEM analysis reveals a flake like morphology. Relating the size of the scale with the size of the particle in the nanofluid, the latter is estimated to be of the order of 10nm. To evaluate the magnetic properties of both nanofluid ferromagnetic carbon/graphite and ferromagnetic carbon/graphite samples, we performed the standard zero field cooled (ZFC) measurements using a MPMS-5T SQUID magnetometer from Quantum Design. Results show the effective ZFC curves for nanofluid ferromagnetic carbon/graphite and ferromagnetic carbon/graphite samples (taken under the applied magnetic field of 1.0kOe) after subtraction of the paramagnetic contributions. Notice that both samples exhibit magnetization curves typical for ferromagnetic materials with the onset Curie temperatures around 300K. Thus, we can conclude that the aqueous suspension of carbon (i.e. nanofluid ferromagnetic carbon/graphite) does not affect the room-temperature magnetization of the ferromagnetic carbon/graphite sample. Given an average value of 10nm for particle sizes in both samples (deduced from TEM images), the low-temperature anomalies observed for both samples are most likely related to the finite size effects. Besides, the results, showing M-H curves at 2K and 300K, the hysteresis does not disappear with increasing temperature and manifests itself in non-zero values of remnant magnetization and coercive magnetic field (HC). Consequently, we can conclude that, even though the material has a relatively small value of HC, it does exhibit a true ferromagnetic behavior up to 300K.

3.4 BIONANOCOMPOSITES AND FERROMAGNETIC CARBON/GRAPHITE: POTENTIAL SYSTEM FOR DRUG DELIVERY[8].

(a) Starting materials and reagents.

Alginate (ALG) and sodium ibuprofen (IBU) were purchased from Sigma–Aldrich. Aqueous solutions were prepared from chemicals of analytical reagent grade: $AlCl_3 6H_2O$ (>99%, Fluka), $MgCl_2 6H_2O$ (Panreac), NaOH (98%, Fluka), NaCl (>99%, Sigma– Aldrich), Na_2CO_3 (>99%, Merck), NaH_2PO4H_2O (>99%, Sigma–Aldrich) and $CaCl_2$ $2H_2O$ (>99%, Sigma–Aldrich). Bidistilled water (resistivity of 18.2MVcm) was obtained with a Maxima Ultrapure Water from Elga. Ferromagnetic carbon/graphite (MG) was synthesized as described elsewhere.

(b) Synthesis of the layered double hydroxide/ibuprofen intercalation compound.

The intercalation compound of IBU in a $[Mg_{0.67}Al_{0.33}(OH)_6]$ $Cl_{0.33}nH_2O$ (Mg_2Al-chloride) LDH was synthesized by the co-precipitation method at constant pH. A mixture of $MgCl_2 6H_2O$ (18 mmol) and $AlCl_{3.6}H_2O$ (9 mmol) was dissolved in 400mL of decarbonated bidistilled water. This aqueous solution and 1 M NaOH solution were added dropwise to 100mL of aqueous solution containing 0.5g IBU using a DOSINO pH module 800 (Metrohm). This system permitted a controlled addition of solutions to maintain a constant pH of around 9.0 during the synthesis. The resulting suspension was kept under nitrogen flow to remove CO_2 and under magnetic stirring for 48h at 60°C. The solid product was isolated by centrifugation, washed several times with bidistilled water, and dried overnight at 60°C. The resulting hybrid material was denoted as LDH–IBU.

(c) Preparation of alginate–ferromagnetic carbon/graphite bionanocomposite beads.

Beads of the alginate–ferromagnetic carbon/graphite bionanocomposites were prepared according to the following procedure: an aqueous solution of 2% (w/v) alginate was magnetically stirred with 1% (w/v) of pure IBU or the necessary amount of LDH–IBU intercalation compound containing 1% (w/v) IBU until homogenization. Then, a stable dispersion of 0.004% (w/v) ferromagnetic carbon/graphite in bidistilled water was added to the alginate solution and homogenized by sonication. This mixture was introduced in a burette and then slowly poured as small droplets into a solution of 15% $CaCl_2$ for 3h. The resulting beads were filtered and washed with abundant doubly distilled water to remove non-entrapped IBU and residual Ca^{2+} ions, frozen in liquid nitrogen and lyophilized in a freeze dryer (Cryodos, Telstar) for later use. The beads containing pure IBU were denoted as ALG/IBU/MG, and those containing LDH–IBU as ALG/LDH–IBU/MG. For comparison, other batches without ferromagnetic carbon/graphite nanoparticles were prepared following the same procedure except for the addition of the ferromagnetic carbon/graphite suspension. The resulting beads were denoted as ALG/IBU when incorporating IBU alone and as ALG/LDH–IBU when the hybrid was added. The initial amount of IBU and MG per gram of alginate in the preparation of the alginate-based beads are summarized in Table 2.

(d) Preparation of alginate–ferromagnetic carbon/ graphite bionanocomposite films.

Films of the alginate-based bionanocomposites with different formulations were produced from the alginate and alginate/MG suspensions loaded with IBU or LDH–IBU, described in the previous section, using a casting/solvent evaporation technique. The different gels were poured into Petri dishes and allowed to dry for 72h at room temperature. Then, the films were gently removed and cross-linked by 5% (w/v) $CaCl_2$ for 15min, washed and finally dried at room temperature.

(e) Characterization powder x-ray diffraction.
X-ray diffraction data were collected in a Bruker D8-ADVANCE diffractometer using a CuK source, with a scan step of 2min between values of 2 and 70. Fourier transfer infrared (FTIR) spectra were recorded with a FTIR spectrophotometer Bruker IFS 66 v/S. Each sample was placed in the sample holder as KBr pellets and scanned from 4000 to 250cm^{-1} with 2cm^{-1} resolution. The amount of organic matter in the LDH intercalation compound was determined by CHN elemental chemical microanalysis in a Perkin Elmer 2400 series II CHNS/O elemental analyzer. The thermal behavior of the diverse prepared materials was analyzed from the simultaneously recorded thermogravimetric (TG) and differential thermal analysis (DTA) curves in a SEIKO SSC/5200 equipment, in experiments carried out under air atmosphere (flux of 100mL min) from room temperature to 1000°C at 10°C min heating rate. Surface morphology was observed in a ZEISS DSM-960 microscope working at 15kV and FE-SEM equipment FEI-NOVA NanoSEM 230. The magnetic behavior of the samples was done by using a SQUID magnetometer from Quantum Design, equipped with a 5T coil. Magnetization vs. temperature curves were conducted following a zero-field cool-field cool (ZFC-FC) protocol (H_{cool} = $H_{measure}$ = 1000Oe). The isothermal field dependence of the magnetization was measured at 5.0K and 300K. The diamagnetic contribution was calculated from the high field slope of the 300K hysteresis cycle and subtracted from the isotherms and the M vs. T curves.

(f) Mechanical properties.
To verify the mechanical properties of dry and wet films, a stress-strain test was executed with a Model 1122 Instron Universal Testing Machine (Instron Corp., Canton/MA, USA). The films were cut to have rectangular dimensions (100mm 5mm) by the ASTM D882-97 test. The dry films were conditioned at 30% RH and 25°C for 48h before measurements and the moisturized films were then immersed in bidistilled water for 2h before the study. The maximum tensile strength (TS), maximum percentage elongation at break (EB%), and elastic modulus (or Young's modulus) were determined. Films were stretched using a speed of 50mm/min. Tensile properties were calculated from the plot of stress (tensile force/initial cross-sectional area) vs. strain (extension as a fraction of the original length). The mechanical properties were analyzed as a function of ferromagnetic carbon/graphite present in the batches. All the experiments were conducted five times.

(g) Estimation of IBU loading and encapsulation efficiency of the beads.
Weighed bionanocomposite beads (0.1g) were immersed in 50mL of 2M phosphate buffer pH 7.4 for 12h. Then, the solution was filtered and the IBU content was calculated from the absorbance measured at λ= 262nm with a UV–vis spectrophotometer (Shimadzu UV-2401), using quartz cuvettes with a 1cm path length. The estimation of the drug percentage loading and the encapsulation efficiency were obtained using the following equations:

$$\%\text{drug loading} = \frac{\text{amount of drugin beads}}{amount\ of\ beads} * 100$$

$$\%\text{encapulation efficiency} = \frac{\text{drug loading}}{theoretical\ \text{loading}} * 100$$

In the second equation, the theoretical loading refers to the initial amount of ibuprofen used in the preparation of the beads indicated in Table 2. All the experiments were carried out in triplicate.

(h) Water uptake studies.
Aliquots of each system of bionanocomposite beads (0.05g) were placed in a Petri dish, immersed in 2M phosphate buffer pH 7.4, and shaken eventually at room temperature. After a predetermined time interval, the beads were withdrawn and weighed on an analytical balance after removing the excess of water. The water uptake was calculated from following equation:

$$\text{water uptake(mg/mg)} = \frac{W_2 - W_1}{W_1}$$

where W_2 and W_1 are the wet and initial mass of beads or films, respectively. This experiment was performed similarly for the films, with a mass of 0.05g in all the batches. All the experiments were carried out in triplicate.

(i) In vitro IBU cumulative release studies.
In a standard study, bionanocomposite beads (0.1g) were added to 50mL of release medium (2 M phosphate buffer solution pH 7.4) and bionanocomposite films (1cm × 1cm) with a mass of 0.1g were added to 15mL of the same release medium, both in thermostatic baths at 37°C. The release study was carried out for 8h. After 30min intervals, 3mL of each medium were withdrawn and the amount of IBU released from the drug-loaded materials was analyzed by UV spectrophotometry (λ= 262nm), and finally, the measured sample was added back to the solution. To evaluate the drug release profile of the magnetic bionanocomposite under magnetic stimulation, a magnetic field (1T) was applied during the release study. The magnet was positioned just beside the flask and was maintained unchangeable under the whole in vitro release process. All the experiments were carried out in triplicate.

4. Results and Discussions

In this section, we show analyze and discuss all results obtained from every experimental method related to (a) the synthesis and characterization of stable room temperature bulk ferromagnetic carbon/graphite; (b) the intrinsic nature, (c) the nanofluid behavior, (d) the potential for building a drug delivery system and (c) the potential use for imaging diagnosis of carbon-based nanostructured magnetic material. By performing a sufficient analysis, we answer here all research open questions.

4.1 PHYSICAL AND STRUCTURAL RESULTS[2,3,4,6,7].
This ferromagnetic carbon/graphite was produced by the reaction of pristine carbon with controlled amounts of oxygen released from the decomposition of CuO at high temperatures. This chemical attack created pores and stacking structures and increased the exposed edges of the graphene planes, producing a foamy-like carbon. The removed carbon may also recrystallize on the carbon crystallite surfaces at the same crucible, thus creating the so-called lower region.

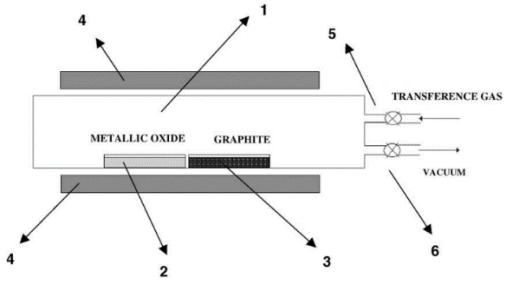

Figure 1: Sketch of the experimental reactor. (1) Closed atmosphere, (2) CuO crucible, (3) carbon crucible, (4) tube furnace, (5) gas input, (6) vacuum.

This vapor phase reaction took place in an inert gas environment. In this case, both N_2 and Ar have been used with similar results, discarding the specific role of N_2 as a reagent or catalyst. The use of powder carbon as a reagent seems to be crucial because of the high reactivity to chemical attacks, due to the high exposed surface and the previous existence of defects. The results did not indicate a significant increase of metallic impurities concerning the original pristine carbon, enough to be responsible for the magnetic properties observed. If these impurities had been the cause of the magnetic effect here reported, both carbon samples, the modified and the pristine ones, should exhibit the same magnetic behavior, which is not the case. A possible explanation for the increase of the impurity's concentration observed especially in iron (approximately 50%) could be the carbon evaporation and recrystallization process in the synthesis here described. Fig. 2 shows the x-ray diffraction profile for the pristine and the modified carbon. A minor shift towards lower d-spacings is detected, in particular for the (002) and (004) reflections. The peaks of the modified carbon are wider and asymmetric, suggesting less crystallinity of these specimens and/or the possible coexistence of regions with different c-axis values. This fact could explain the difficulty found to unambiguously determine the c cell parameter. Despite this, the inset could be evidence of the c-axis compression suggesting a carbon structure with defects that would have the effect of getting the graphene layers closer.

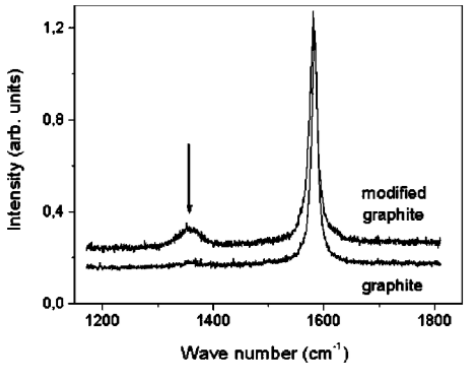

Figure 2: Raman spectra of the pristine and modified ferromagnetic carbon/graphite samples.

Micro-Raman analysis (Fig. 2) of the pristine carbon exhibited a peak at 1580cm^{-1}, showing the good quality of the reagent used in this procedure. The modified ferromagnetic carbon/graphite clearly showed the occurrence of the 1350cm^{-1} peak, well known as the "disordered" D band. A broadening of the 1580cm^{-1} peak was also observed. Both signals are indicative that the crystal could no longer be regarded as infinite, and that the presence of defects is clearly significant. The presence of magnetic regions at the microscale has been verified by MFM. Also, the role of the pores and the microstructural features were studied simultaneously with atomic force AFM and magnetic force microscopy MFM, trying to correlate the topography to the magnetic signal.

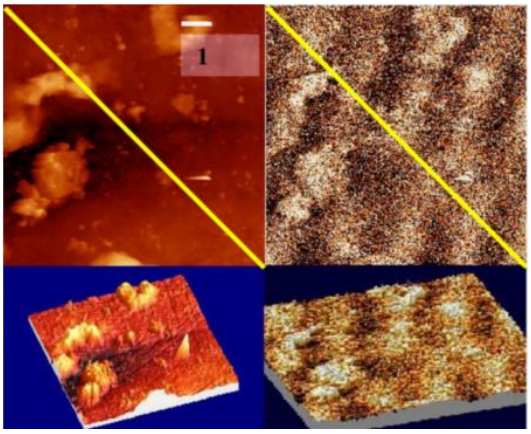

Figure 3: Set of images of an area of a ferromagnetic carbon/graphite sample of 10mm × 10mm corresponding to the topography AFM, upper left imaged and the magnetic behavior MFM, upper-right imaged. At the bottom we show the corresponding 3D images.

Fig. 3 shows a 10mm × 10mm picture of the topography super-left imaged of one of the ferromagnetic carbon/graphite samples, and the corresponding magnetic behavior MFM, upper-right imaged. A large pore can be seen at the topography image, and a grid scheme typical of magnetic systems is clearly seen surrounding it, where magnetic domains are fairly homogeneously distributed. The periodicity of the domains is approximately 1mm. At the bottom of those figures we show the corresponding three-dimensional 3D images.

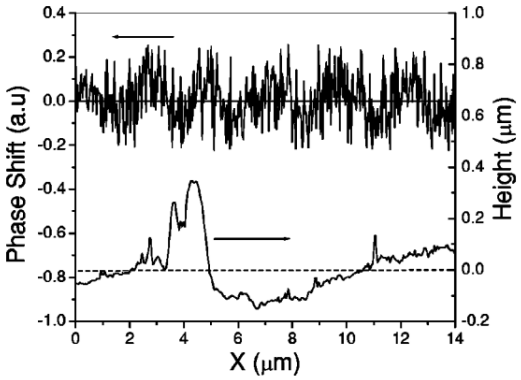

Figure 4: Diagonal profile section corresponding to the lines depicted on the top images of Fig. 2 and related to the height (topography) and to the phase-shift (magnetic) signals.

Fig. 4 shows the diagonal profile section corresponding to the lines depicted on top images of Fig. 3 of both the topography and the magnetic signal keeping outside most of the pored. Its analysis clearly allows us to stress that the magnetic signal is not correlated to the roughness of the sample surface outside the pore, i.e., the origin of the magnetic grid is genuinely intrinsic.

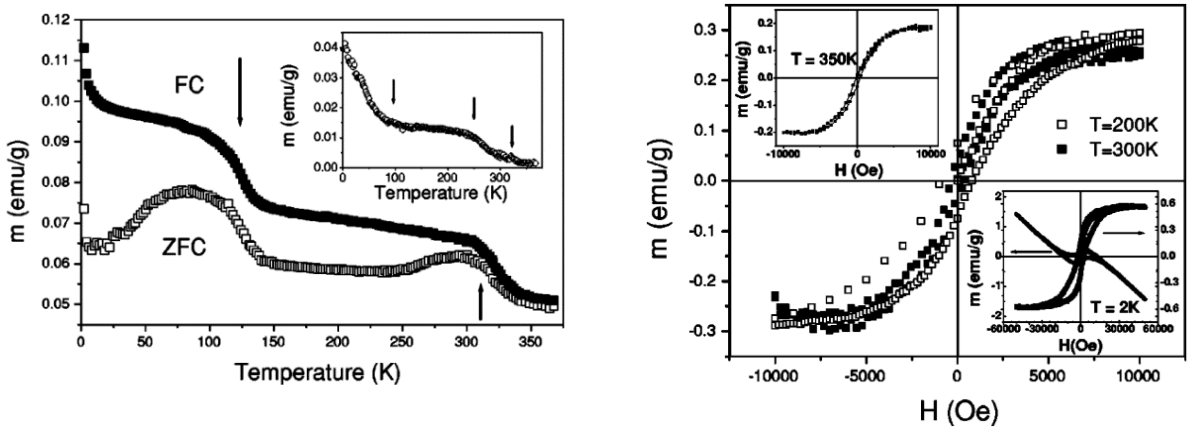

(a) (b)

Figure 5: (a) ZFC and FC magnetization vs temperature. The arrows show the magnetic transition temperatures. Inset: the difference in the magnetization FC-ZFC vs temperature. The arrows show changes of slopes; (b) hysteresis curves, m vs H, for the ferromagnetic carbon/graphite material for T=200K and 300K. Lower right inset: m vs H at 2K, with and without the diamagnetic background subtraction. Upper left inset: m vs H at 350K.

Fig. 5 shows the magnetic behavior of ferromagnetic carbon/graphite. Fig. 5(a) shows the magnetic moment (m) as a function of temperature, T (zero field cooled ZFC and field cooled FC for H=1000 Oe). Two clear magnetic transitions are observed: T_{c1}=115K and T_{c2}=315K. The irreversibility of the system is clear and can be better seen in the inset, where the difference between the magnetization values at the FC and ZFC branches is plotted against temperature. The arrows in the inset show changes in slopes, which are a few degrees below the magnetic transitions. There is evidence of the persistence of ferromagnetism even at 350K, where a weak loop can still be observed at the upper-left inset of Fig. 5(a). This multilevel ferromagnetic behavior, evidenced by several Curie temperatures, could be explained through the inhomogeneity of the modified ferromagnetic carbon/graphite specimen derived from the presence of defects, as stated by both MFM and Raman experiments. As a consequence of the defects created, the material becomes inhomogeneous, which seems to be an essential feature of the ferromagnetic carbon/graphite samples. The presence of ferromagnetic islands, related to the inhomogeneity of defects, is supported by the high irreversibility observed in the m vs T plot. In principle, the complex magnetic behavior should be intrinsic and could not be avoided. Due to the defects created, the material enhances the intrinsic magnetic behavior previously reported. The use of powder carbon as a reagent seems to be crucial because of the high reactivity to chemical attacks, due to the highly exposed surface, and the previous existence of defects. Thus, the concentration of defects produced by chemical attack could be the cause of producing the strong magnetic response reported here. Fig. 5(b) exhibits the hysteresis cycle for the m vs H curves at 2, 200, 300, and 350K. The lower right inset also shows the m vs. H loop at 2K without the subtraction of the diamagnetic background.

We assumed that the material at 2K lacked the paramagnetic phases and used this curve to establish the diamagnetic contribution to be subtracted at all temperatures (approximately -3×10^{-5} emu/g). Then, a paramagnetic contribution was also subtracted at 200, 300, and 350K. The saturation magnetic moment was strong, 0.58, 0.28, 0.25, 0.19 emu/g, for T=2, 200, 300, and 350K, respectively. The saturation magnetization at 2K, leads to a defect concentration of 1250 ppm, assuming that each defect has a magnetic moment $g\mu_B S$ (with g=2, S= ½). This value is higher than others previously reported, such as the 78–840 ppm range for nanocarbon-based carbon materials.

To justify those values of the saturation magnetic moment through the role of magnetic impurities by assuming that all these impurities behave as bulk ferromagnetic material— which most probably would not be the case— it would require a ferromagnetic cluster of about 2600 ppm of Fe. As previously mentioned, the total content of iron in our samples was determined to be around 40–60 ppm range (spread, not in a cluster). Other ferromagnetic metals such as nickel and cobalt were detected at concentrations around 1 ppm. Since this value is much lower than the one required, the presence of ferromagnetic impurities cannot be responsible for the magnetic behavior of this material, and this hypothesis can be ruled out. A strong decrease in the coercive field was observed when temperature increases, HC=2200, 850, 350, and 170 Oe at 2, 200, 300, and 350K, respectively. The remnant magnetization was 0.17, 0.075, 0.04, and 0.01 emu/g for 2, 200, 300, and 350K, respectively. These values correspond to 29, 27, 16, and 5% of the saturation magnetic moment for 2, 200, 300, and 350K, respectively.

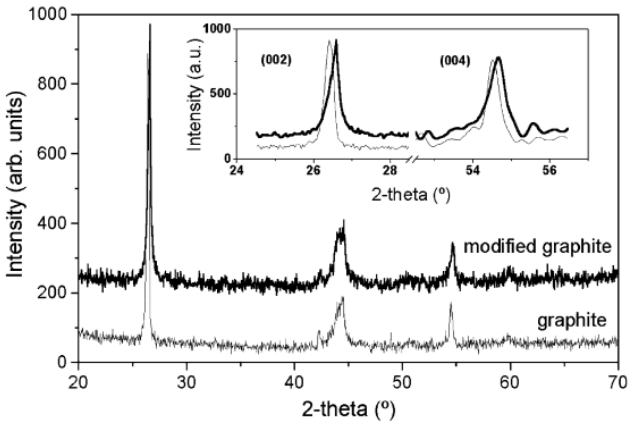

Figure 6: X-ray diffraction profiles of pristine and modified carbon. The inset shows the details of the (002) and (004) reflections regions (smoothing has been applied to the (004) region, for clarity).

X-ray diffraction analysis on this material suggested the coexistence of a nonmagnetic pristine carbon matrix and foamy carbon with decrease of the *d* spacing of the (001) reflections. Fig. 6 shows the x-ray diffraction profile for the pristine and the modified carbon. A minor shift towards lower d-spacings is detected, in particular for the (002) and (004) reflections. In fact, the peaks of the modified carbon are wider and asymmetric, suggesting less crystallinity of this specimens and/or the possible coexistence of regions with different c-axis values. This fact could explain the difficulty found to unambiguously determine the c cell parameter. In spite of this, the inset could be evidence of the c-axis compression suggesting a carbon structure with defects that would have the effect to get the graphene layers closer.

Fig. 7 exhibits SEM micrographs have given enough evidence about the topological changes occurring at the micro-structural scale. Those micrographs from the pristine carbon powder used as reagent and the processed material, respectively. Fig. 7b shows a carbon grain after chemical attack, exhibiting a pore. The pores exhibit a large dispersion of sizes with diameters ranging from a few nanometers to approximately 1mm.

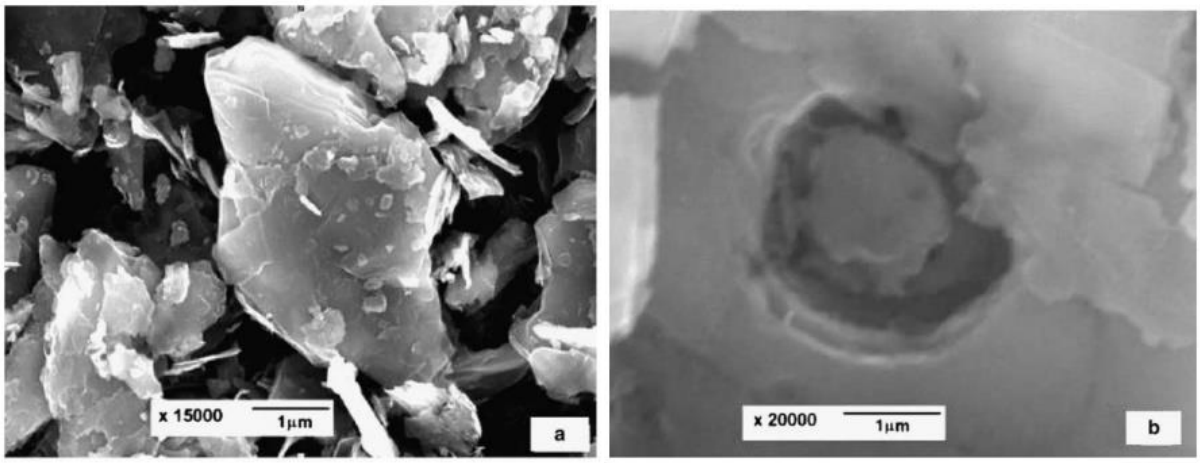

Figure 7: SEM images of the morphology of (a) the carbon used as reagent; (b) one pore in the modified carbon, 1mm diameter—the propagation of the pore along the lamellar structure can be seen.

Figs. 8 and 9 exhibit the experimental results related to the obtention of nanofluid ferromagnetic carbon/graphite. Fig.8 shows the Raman spectra for ferromagnetic carbon/graphite, the surfactant used in the suspension (CTAB), and the aqueous suspension of the nanofluid ferromagnetic carbon/graphite. It revealed the presence of the peak at 1650cm^{-1} corresponding to nanofluid ferromagnetic carbon/graphite, in addition to the peak at 1350cm^{-1} (known as the "disordered" D band) in the ferromagnetic carbon/graphite sample. For further comparison, Fig. 8 depicts the Raman spectrum showing characteristic bands of the surfactant used in the suspension (CTAB). Observe that, as expected, the CTAB functional groups, the hydrophobic (carbonic chain) and hydrophilic (cationic-active tensions with positive charge) parts of the surfactant correlate with the band structure of the pure carbon. Since the hydrophilic part tends to bind with the water molecules, its action results in stabilization of the nanofluid suspension. The structural characterization of nanofluid ferromagnetic carbon/graphite was performed by transmission electron microscopy (TEM) using Philips CM-120 microscope.

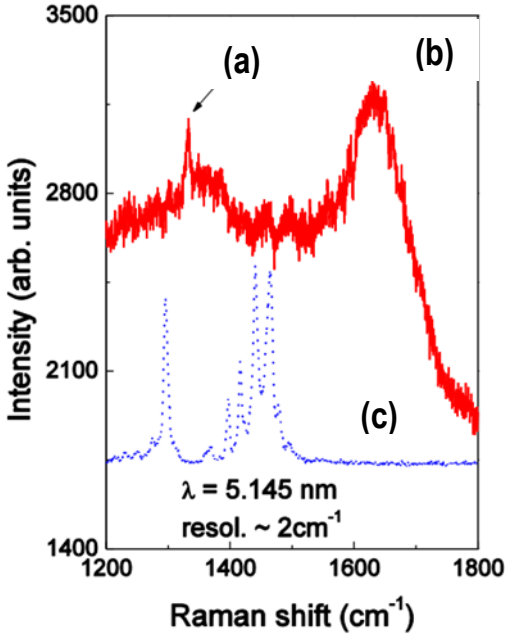

Figure 8: Raman spectra showing in the upper curve (a) the picks for ferromagnetic carbon/graphite and (b) the nanofluid ferromagnetic carbon/graphite, and in the lower curve (c) the peaks for the surfactant used in the suspension, CTAB.

Fig. 9 shows TEM analysis revealing a flake like morphology of nanofluid ferromagnetic carbon/graphite sample. Relating the size of the scale in Fig. 2 with the size of the particle in the nanofluid ferromagnetic carbon/graphite, the latter is estimated to be of the order of 10nm. To test the magnetic properties of both ferromagnetic carbon/graphite and nanofluid ferromagnetic carbon/graphite samples, we performed the standard zero field cooled (ZFC) measurements using a MPMS-5T SQUID magnetometer from Quantum Design.

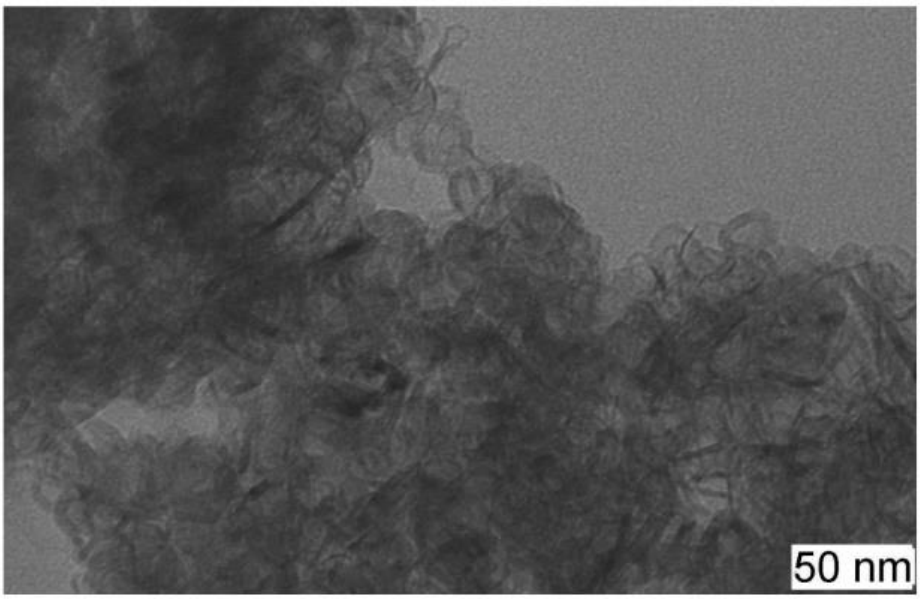

Figure 9: TEM (transmission electron microscopy) image of nanofluid ferromagnetic carbon/graphite sample showing a flake-like structure with an average size of the particle of the order of 10nm.

Fig. 10 presents the effective ZFC curves for ferromagnetic carbon/graphite and nanofluid ferromagnetic carbon/graphite samples (taken under the applied magnetic field of 1kOe) after subtraction of the paramagnetic contributions. Notice that both ferromagnetic carbon/graphite and nanofluid ferromagnetic carbon/graphite samples exhibit magnetization curves typical for ferromagnetic materials with the onset Curie temperatures around 300K. Thus, we can conclude that the aqueous suspension of carbon (i.e., nanofluid ferromagnetic carbon/graphite) does not affect the room-temperature magnetization of the ferromagnetic carbon/graphite sample. Given an average value of 10nm for particle sizes in both ferromagnetic carbon/graphite and nanofluid ferromagnetic carbon/graphite (deduced from TEM images), the low-temperature anomalies seen in Fig.10 for both samples are most likely related to the finite size effects. Besides, according to Fig.11 (which shows M-H curves at 2K and 300K), the hysteresis does not disappear with increasing the temperature and manifests itself in non-zero values of remnant magnetization and coercive magnetic field (HC). Consequently, we can conclude that, even though the material has a relatively small value of H_C, it does exhibit a true ferromagnetic behavior up to 300K.

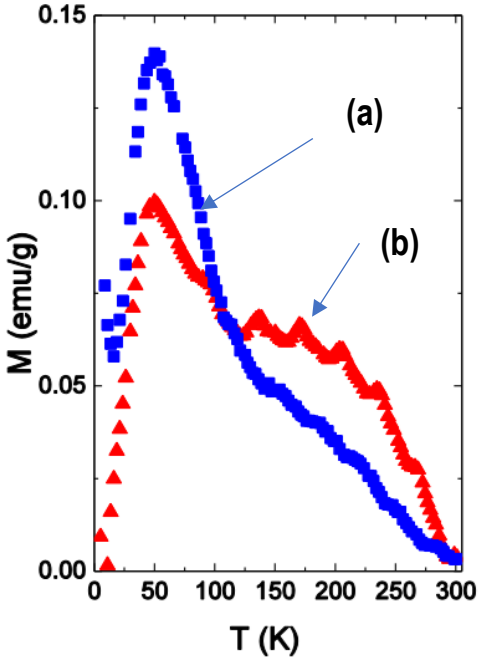

Figure 10: The temperature dependence of the effective ZFC magnetization for (a) ferromagnetic carbon/graphite and (b) nanofluid ferromagnetic carbon/graphite samples (after subtracting the paramagnetic contributions).

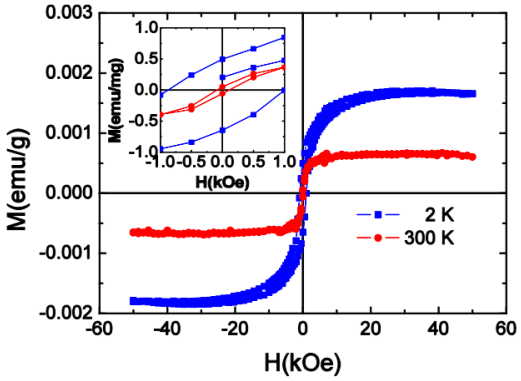

Figure 11: The hysteresis curves for nanofluid ferromagnetic carbon/graphite sample for two temperatures (2K and 300K) showing a ferromagnetic like behavior of the sample. Inset: low-field M-H curves.

4.2 DFT AND NMR RESULTS[5].

(a) Electronic structure calculations.

Without any a priori information about the hyperfine field, it would be difficult to find the zero-field nuclear resonance signal. Thus, a series of first-principles calculations based on DFT was carried out to guide the NMR experiment. Calculations were performed in nanosized model systems built to somewhat reproduce the local features of the structure of ferromagnetic carbon/graphite (Fig. 11). The model systems included graphene sheets with isolated or multiple single atomic vacancies, as well as carbon nanoribbons with oxygen atoms adsorbed at the zigzag edge sites. These systems are known from previous reports to give rise to magnetic moments localized at carbon atoms, with indications of a ferromagnetic ground state in some cases, and thus they were considered good candidates for the initial calculations of B_{hf} at ^{13}C nuclei.

Table 1: Calculated hyperfine magnetic field (B_{hf}) in ferromagnetic carbon-based systems. The reported values correspond to the average taken over the sites where the largest magnetic moments were located in each system.

System	B_{hf}(T)
Graphene sheet with one single vacancy (System A)	19.4
Graphene sheet with one single vacancy (System B)	18.8
Graphene sheet with two single vacancies (System C)	18.3
Graphene sheet with two single vacancies (System D)	20.2
Graphite nanoribbon (System E)	20.8

A summary of the results of the DFT calculations is presented in Table 1. The first noticeable aspect of these results is that all values fall into the same range, ~ 18–21T, despite the different types of defects giving rise to magnetism in vacancy-containing graphene sheets and in oxygen-containing carbon nanoribbons. This is an indication that the B_{hf} values here reported are indeed characteristic of carbon sites with localized magnetic moments in carbon-based systems. As it should be expected, the largest B_{hf} values in each system were found at the sites also presenting the highest net spin densities and, thus, the largest atomic magnetic moments, as illustrated in Fig. 12 for some of the studied systems. There are some variations in the average B_{hf} values as well as in the total magnetic moments of each system due to the possible interactions between neighbor atomic magnetic moments. As an example, the comparison between systems containing a single atomic vacancy (systems A and B, as described in Table 1 and with supercells exhibited in Fig. 11) shows a slightly reduced B_{hf} value for the larger supercell, corresponding to the larger separation between each defect and its image produced by the use of periodic boundary conditions in the calculations.

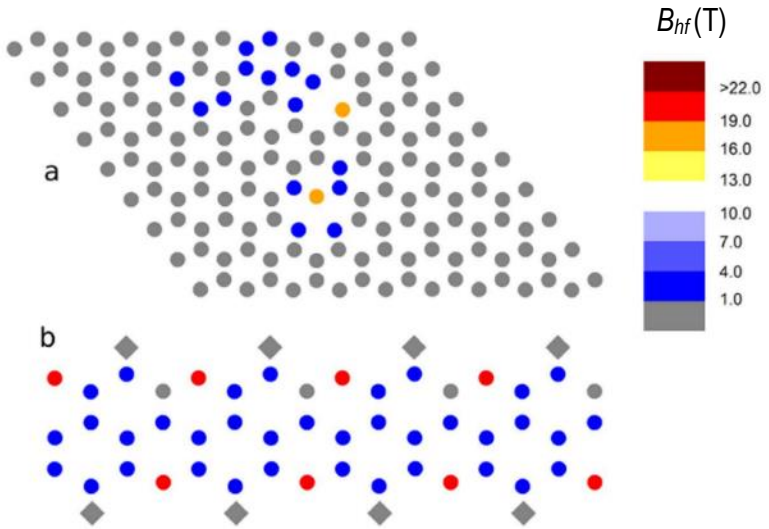

Figure 12: Colormaps showing the distribution of calculated B_{hf} values. (a) for system C (graphene sheet with two atomic vacancies ca. 11Å), and (b) along a single graphene layer in system E (carbon nanoribbon). The circles represent carbon atoms and the diamonds in (b) represent oxygen atoms.

Similarly, in the case of two interacting single vacancies (systems C and D), the B_{hf} value and the total magnetic moment were found to increase with the reduction in the separation between the two ferromagnetically coupled vacancies. The largest total magnetic moments and B_{hf} values among the studied systems were found for the carbon nanoribbon, where the magnetic response is the result of the ferromagnetic coupling between the magnetic moments associated with dangling bonds at edge sites. It is important to stress here that none of these models is supposed to describe in detail the structural features of bulk ferromagnetic carbon/graphite. The details about the structure and the mechanism leading to the emergence of the magnetic properties in this material remain to be elucidated, in spite of previous insights about the role played by oxygen-induced defects. The use of the carbon nanoribbon with oxygen atoms at the edges in the DFT calculations is simply one of many possibilities to model an oxygen-containing graphitic system having structural defects and presenting a ferromagnetic ground state, as previously shown by theoretical calculations. However, the results of the DFT calculations show that irrespective of the specific structural defect present in each one of the modeled systems, the local magnetic moment and the hyperfine magnetic field remain nearly constant. Thus, the present calculations are thought to represent well the local neighborhood of structural defects in ferromagnetic carbon materials, at least from the point of view of the hyperfine magnetic coupling.

(b) NMR measurements and comparison to theoretical DFT predictions.

Guided by DFT calculations mentioned before, zero-field NMR experiments were carried out in a frequency range encompassing the resonance frequencies corresponding to the predicted B_{hf} values.

Taking the predicted hyperfine field from DFT data shown in Table 1, using the proportionality between nuclear magnetic resonance frequency and hyperfine field:

$$n_{zfNMR} = gB_{hf}$$

and the well-known magnetogyric ratio of ^{13}C:

$$g = 10.569 \text{ MHz/T}$$

Then, the resonance frequencies were estimated to be in the range 200–230MHz.

A significant zero-field NMR signal was indeed found at frequencies just above this range at 1.5K by sweeping the frequency. We employed the standard two-pulse NMR technique known as spin echoes, where specific radio-frequency pulses are used to refocus the nuclear magnetization at a moment in time (Fig. 13a).

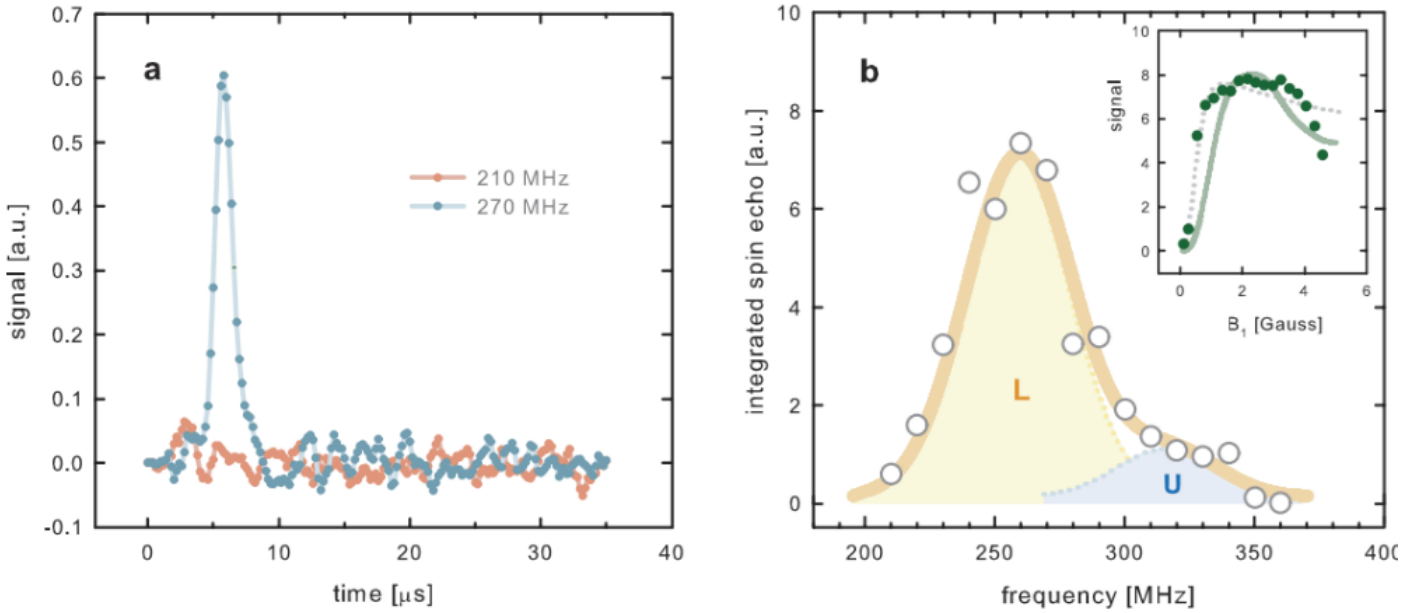

Figure 13: Zero-field ^{13}C NMR in ferromagnetic carbon/graphite. (a) Raw time-domain zero-field NMR signal due to ^{13}C nuclei in ferromagnetic carbon/graphite at two frequencies (red circles 210MHz, blue circles 270MHz); (b) ^{13}C zero-field NMR spectrum, obtained by integrating spin echoes at different frequencies, at 1.5K.

The spin echo signal is unique of magnetic resonance, eliminating possible artefacts (as clearly demonstrated with the 'blank' measurement at 210MHz). The maximum signal was detected at 260MHz, as shown in the NMR spectrum exhibited in Fig. 13b. The B_{hf} value corresponding to this peak is around 24T. The deviation from the calculated values given in Table 1 is not surprising, considering the complexity of the real material (from the chemical, structural and magnetic point of view) in comparison to the idealized model systems used in the DFT calculations. The sizeable width of the zero-field NMR line indicates that a hyperfine field distribution exists within the material, which is also qualitatively in agreement with calculations. The zero-field NMR spectrum shown in Fig. 13b was fitted with two Gaussian lines, named lower (L) and upper (U) lines, with different intensities (L being thus the dominant contribution in zero-field NMR spectra). The two lines may originate from sites with different local fields – corresponding to different types of defects – or from nuclei in different domain wall environments. The two lines in the inset of Fig. 13b are the 'drumhead' model of NMR enhancement in domain walls (modeling the domain wall motion in the applied RF field as vibrating drumheads – dotted line) and a model with strong domain wall pinning anisotropy (due to the graphene-like layers in the carbon structure – full line). Domain wall dynamics in ferromagnetic carbon/graphite is thus interesting in itself, warranting further investigation (for more details on the enhancement models see Supplementary Information). A zero-field carbon NMR signal was also detected at temperatures significantly higher than 1.5K (Fig. 14), establishing some correspondence with the high-temperature ferromagnetism observed previously in ferromagnetic carbon/graphite.

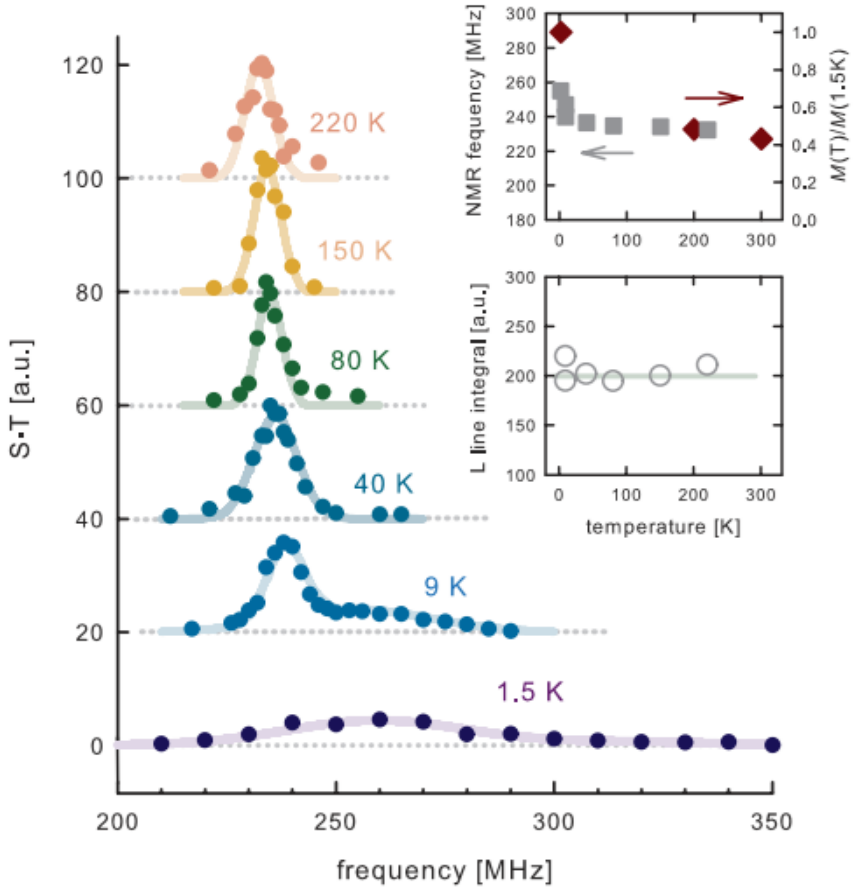

Figure 14: Temperature dependence of the zero-field NMR spectrum of ferromagnetic carbon/graphite. Upper inset: comparison of the L line NMR frequency and saturation magnetization normalized to the low-temperature value. Lower inset: integrals of the L lines from the main figure, in dependence on temperature.

Previous reports on the magnetic behavior of ferromagnetic carbon/graphite show that the magnetization does not decrease significantly from 2K up to 300K, and magnetism is still present at 350K. The same general trend was indeed observed for the zero-field NMR frequency of the L line up to 220K (Fig. 14, upper inset), with a noticeable agreement especially at high temperatures. This is also in line with the constancy of L line intensity (Fig. 14, lower inset). Thus, it is clear from these data that the NMR signal and the magnetic response are likely to be produced by the same source (i.e., structural defects). The failure to detect the U line at high temperatures makes difficult a more detailed direct comparison of microscopic NMR data and macroscopic sample magnetization. Namely, the saturation magnetic moment of the sample is proportional to the local magnetization (and thus to the local field) multiplied by the volume fraction of magnetized material. The NMR signal intensity is a measure of the volume fraction, and thus the unknown U line contribution renders a quantitative comparison impossible. The extra magnetization at low temperatures is then plausibly related to the U line signal. An NMR signal above 220K was probably not observed due to spin-spin and spin-lattice relaxation effects, since fluctuations increase as the Curie temperature is approached.

4.3 BIONANOCOMPOSITES AND FERROMAGNETIC CARBON/GRAPHITE RESULTS[8].

The bionanocomposites were prepared by dispersing the pure drug or the LDH–IBU hybrid in alginate, together with pre-synthesized ferromagnetic carbon/graphite nanoparticles using 15% $CaCl_2$ to produce the cross-linking of the biopolymer, affording the formation of magnetic bio-hybrid beads (Fig. 15). With the use of LDH–IBU it is intended to have a better control in the release rate of the drug as proposed by diverse authors.

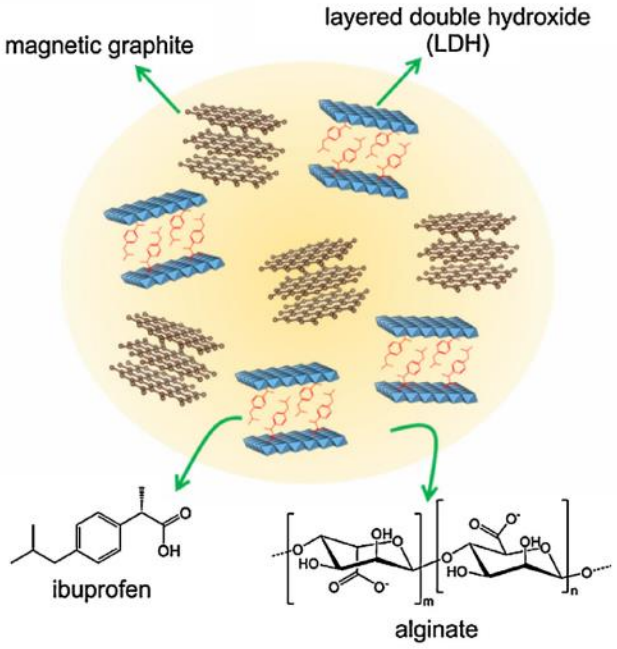

Figure 15: Scheme of the magnetic bionanocomposite system based on ALG/LDH–IBU/MG where MG represents the ferromagnetic carbon/graphite.

Beads of the alginate–ferromagnetic carbon/graphite bionanocomposites were prepared as described before in Section 2. The beads containing pure IBU were denoted

as ALG/IBU/MG (where MG represents the ferromagnetic carbon/graphite), and those containing LDH–IBU as ALG/LDH–IBU/MG. For comparison, other batches without ferromagnetic carbon/graphite nanoparticles were prepared following the same procedure except the addition of the ferromagnetic carbon/graphite suspension. The resulting beads were denoted as ALG/IBU when incorporating IBU alone and as ALG/LDH–IBU when the hybrid was added. The initial amount of IBU and MG per gram of alginate in the preparation of the alginate-based beads are summarized in Table 2.

Table 2: Initial amount of ibuprofen (IBU) and ferromagnetic carbon/graphite (MG) per gram of alginate used in the preparation of the alginate-based beads.

Compositions of samples	Nomenclature of samples	IBU (g)	MG (g)
Alginate encapsulating IBU	ALG/IBU	o.1	0
Alginate–magnetic graphite encapsulating IBU	ALG/IBU/MG	0.1	0.002
Alginate encapsulating LDH-intercalated IBU	ALG/LDH–IBU	0.1	0
Alginate–magnetic graphite encapsulating LDH-intercalated IBU	ALG/LDH–IBU/MG	0.1	0.002

Both the ALG/LDH–IBU bionanocomposite and the IBU-loaded alginate systems have been also implemented with ferromagnetic carbon/graphite nanoparticles (MG) that show a ferromagnetic behavior, with a strong saturation magnetic moment close to 0.25 emu/g at 300K. An important advantage of these carbon nanoparticles is their ability to form stable suspensions in bidistilled water by sonication, without the necessity to add surfactants, organic solvents or acids as reported for other magnetic systems. Thus, MG can be easily dispersed within the biopolymer matrices providing the resulting bionanocomposites with magnetic properties together with hydrophobicity, which can have also a strong influence on the water sorption properties of these materials and, consequently, on the rate of drug release.

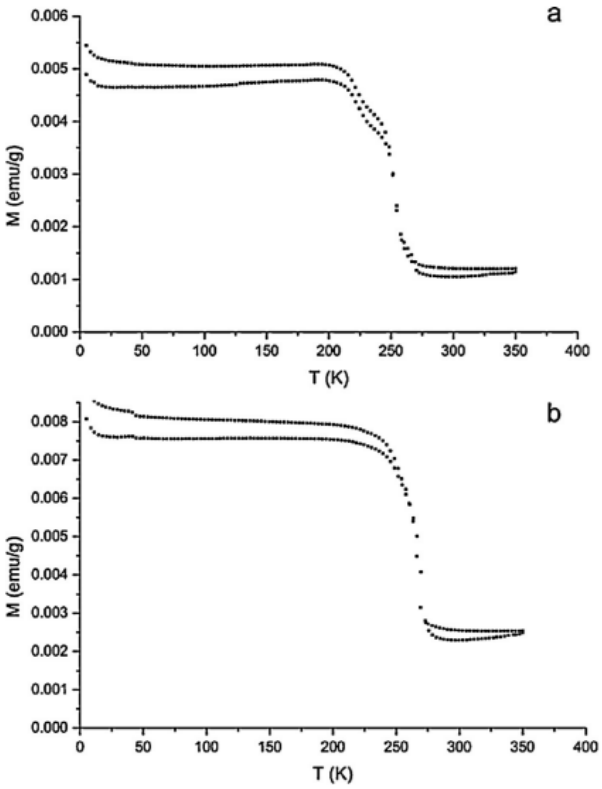

Figure 16: Temperature dependence of the magnetization for (a) ALG/IBU/MG and (b) ALG/LDH–IBU/MG samples.

Fig. 16 shows the ZFC-FC measurements of temperature dependence of the magnetization for both samples ALG/IBU/MG and ALG/LDH–IBU/MG, respectively. The main features, regarding the magnetism reported by Mombrú et al. for the pristine carbon sample, remain as the main ingredient of a multilevel development of the ferromagnetic behavior it is also observed in the bionanocomposite samples here described. However, some differences become apparent: first, the magnetic signal is strongly reduced with respect to that of the pristine ferromagnetic carbon/graphite sample since it is very diluted in the bionanocomposite samples and the data have been normalized to the total mass; second, two main transitions are spotted for sample ALG/IBU/MG, now located at T_{C1} = 237K and T_{C2} around 272K. For sample ALG/LDH–IBU/MG, a clear transition can be seen at T_{C2} = 273K and a small anomaly is also detected at T_{C1} = 45K. It is worth mentioning the T_{C2} is sensitive to the cooling protocol and a decrease of the critical temperature is observed in both samples when cooling in a magnetic field (DT ~ 4K). Large irreversibility is also observed in both samples pointing out to substantial magnetic disorder, as it was reported for the pristine sample. Note that at room temperature both samples remain ferromagnetic (ferromagnetic hysteresis cycles not shown) up to the highest temperatures explored (350K).

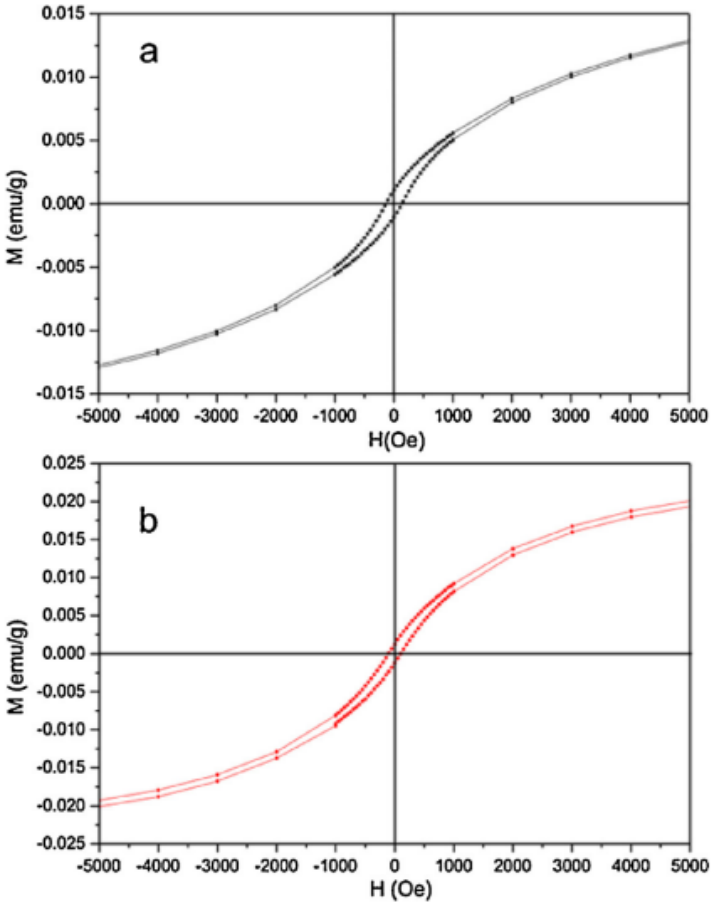

Figure 17: Hysteresis cycles measured at 5K for (a) ALG/IBU/MG and (b) ALG/LDH–IBU/ MG.

Fig.17 shows the hysteresis cycles measured at 5K. As compared to the reported values for pristine carbon, the coercive fields are much smaller for both samples (HC = 150Oe for ALG/IBU/MG and HC = 98Oe for ALG/LDH–IBU/MG). Both samples exhibit a clear ferromagnetic behavior with a finite remanence and a finite coercive field. The high field values of the magnetization are larger for ALG/LDH–IBU/MG than for ALG/IBU/MG. None of the samples saturates as a small paramagnetic contribution is present at low temperatures. Irreversibility is larger for ALG/LDH–IBU/MG. In pristine carbon the observed ferromagnetic behavior was ascribed to the existence of a variety of defects resulting from the vapor phase redox reaction of carbon in a N_2 atmosphere. In this context, differences observed in the temperature and field dependence of the magnetizations in our samples, as compared to the pristine carbon, are to be explained in terms of changes in the number and distribution of defects as a consequence of the ulterior processing of carbon particles into the matrix and also to the appearance of new interactions in the composite.

Table 3: Initial amount of ibuprofen (IBU) and ferromagnetic carbon/graphite (MG) per gram of alginate used in the preparation of the alginate-based beads.

Formulation	IBU loading (%)	Encapsulation efficiency (%)
ALG/IBU	2.73 ± 0.55	30.3 ± 6.1
ALG/LDH–IBU	2.55 ± 0.25	37.6 ± 3.7
ALG/IBU/MG	4.49 ± 0.06	49.9 ± 0.6
ALG/LDH–IBU/MG	4.70 ± 0.17	69.1 ± 2.5

The encapsulation efficiency of the alginate-based DDS and the percentage of drug loaded in different batches of beads with and without the incorporation of MG nanoparticles are listed in Table 3. It is observed that the amount of IBU loaded in the different beads is very similar when the drug is intercalated either directly or within the brucite-like layers, being higher when magnetic nanoparticles are present in both types of matrices. These results suggest that the presence of the MG contributes to increase the encapsulation efficiency, probably due to its hydrophobic character, which would prevent the leaching of the drug during the beads processing, leading to values about twice those of systems without magnetic particles.

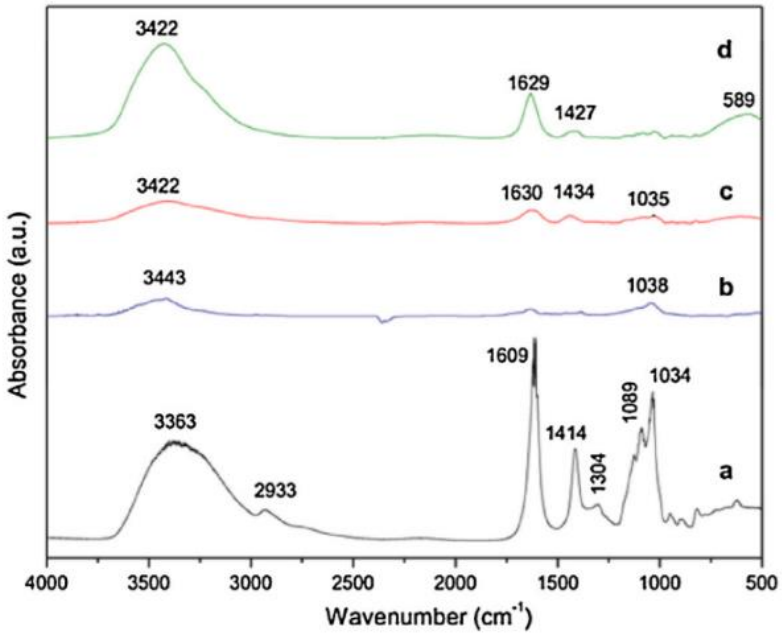

Figure 18: FTIR spectra (4000–400 cm^{-1} region) of pristine alginate (a); pristine ferromagnetic carbon/graphite (b); ALG/MG (c); and ALG/LDH–IBU/MG (d) bionanocomposite beads.

The FTIR spectra of the alginate–ferromagnetic carbon/graphite bionanocomposites incorporating LDH–IBU and IBU are shown in Fig. 18. The spectrum of pristine alginate (Fig. 18a) reveals bands at 3363cm^{-1}, 1609cm^{-1}, 1414cm^{-1} and 1034cm^{-1}, corresponding to n_{OH}(H2O and OH), nas_{CO}(—COO^{-}), ns_{CO}(—COO^{-}) and nas_{CO}(C—O—C) vibration modes, respectively. The spectrum of pure ferromagnetic carbon/graphite (Fig. 18b) shows bands at 1038 and 1637cm^{-1}, attributed to the $d_{C—H}$ and $n_{C—C}$ vibration modes, respectively. The other band at 3443cm^{-1} can be attributed to n_{OH} vibration modes. The spectra of the alginate/MG (Fig. 18c) and the alginate/LDH–IBU/MG (Fig. 18d) beads show a shift of the vibration bands observed in the alginate spectrum at 1414cm^{-1} and 1609cm^{-1} to higher wave-number values in both cases, which is attributed to the existence of ionic interactions between Ca^{2+} ions and the carboxylate groups of alginate as a consequence of the cross-linking process introduced in the formation of the beads. Besides the cross-linking effect, the existence of interactions between the carboxylate groups and the ferromagnetic carbon/graphite nanoparticles should not be discarded, as observed in FTIR studies on the interaction of carbon nanotubes and sodium alginate previously reported. On the other hand, the spectrum of alginate/LDH–IBU/MG beads (Fig. 18d) show a low intensity band at 589cm^{-1} related to the O—M—O bending vibration mode of the brucite-like structural layers, which confirms the preservation of the LDH structure once incorporated in the bionanocomposite beads. The broad band centered at 3422cm^{-1} can be ascribed to the O—H vibrations of hydroxyl groups in alginate as well as in adsorbed water molecules.

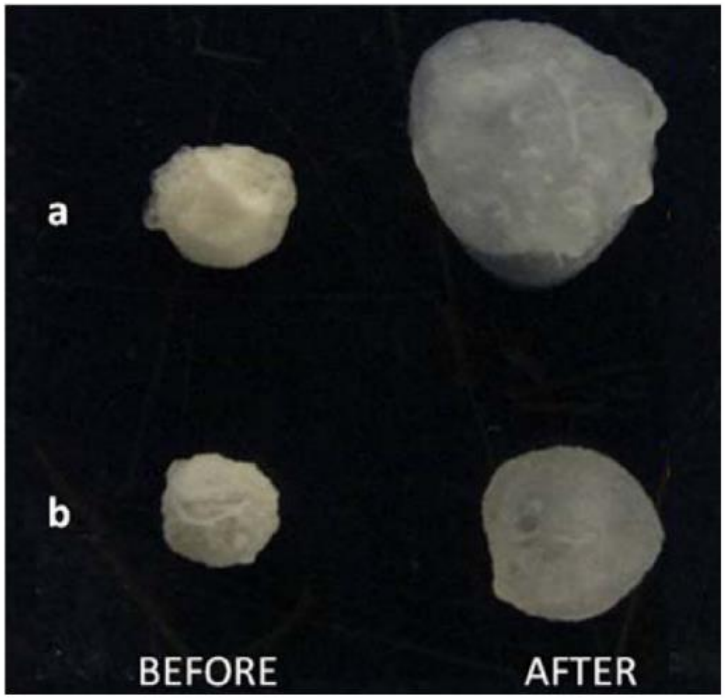

Figure 19: Aspect of the (a) ALG/LDH–IBU and (b) ALG/LDH–IBU/MG bionanocomposite beads before and after immersion in phosphate buffer for 6 h.

The presence of ferromagnetic carbon/graphite nanoparticles significantly changes the behavior of the bionanocomposites. Thus, the bionanocomposite beads containing ferromagnetic carbon/graphite exhibit in all cases lower water absorption values than the ones without MG. The ALG/IBU/MG beads reached an uptake of around 9 g/g of bead, about 16g less than the ALG/IBU beads. This observation confirms the role of inorganic nanoparticles in the bionanocomposite in increasing their stability toward water uptake. Thus, the ALG/LDH–IBU/MG beads presented the lowest water uptake, around 7g of water per gram of beads, due to the presence of the hybrids and the ferromagnetic carbon/graphite nanoparticles in the bionanocomposite. Similarly, ALG/IBU/MG films absorbed only around 9g of water compared to the 12g per gram of film absorbed by the analogous ALG/IBU system without MG. The presence of MG nanoparticles also increased the stability of the bionanocomposites processed as films, as ALG/IBU films disintegrated after 3h of study, while the disintegration of ALG/IBU/MG films occurred after 5h. The water uptake of the ALG/LDH– IBU/MG bionanocomposite film was quite similar to that of the system incorporating IBU directly, reaching a water uptake of 10g/g of film. These results confirm the role of ferromagnetic carbon/graphite in the bionanocomposites which not only improves the mechanical properties but also confers more resistance to water absorption due to its hydrophobic character, acting as a physical barrier at the interface of the bionanocomposite and the medium, even in the batches without the LDH–IBU intercalation compounds. Fig. 19 shows the aspect of the beads before and after swelling in an aqueous medium, with a considerable difference in their size due to the presence of the ferromagnetic carbon/graphite nanoparticles.

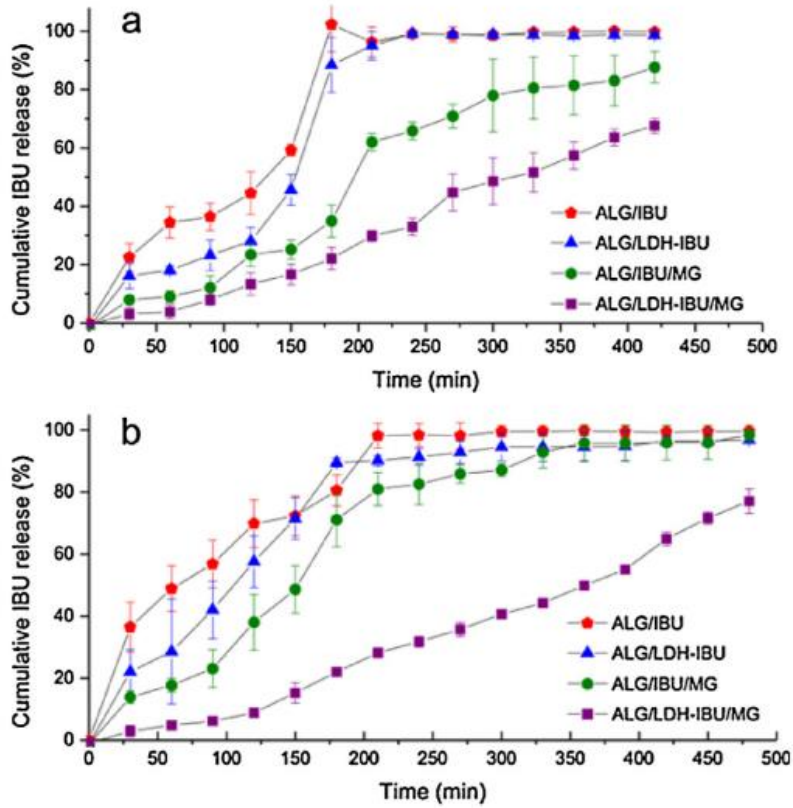

Figure 20: Profile of IBU release from different bionanocomposite (a) beads and (b) films in phosphate buffer pH 7.4 at 37°C.

The medium of the release of IBU, chosen as the model drug in this study, was phosphate buffer pH 7.4 used as a simulated physiological medium. Fig. 20 shows the release profile of all the studied batches, confirming that the presence of ferromagnetic carbon/graphite nanoparticles in the beads slows down the rate of (the) drug delivery, providing a constant release during the whole experiment. The ALG/IBU and ALG/LDH–IBU beads rapidly reached around 99% of release after 3 and 4h of study, respectively (Fig. 20a). These results show that DDS based on alginate are very sensitive to this medium, which facilitates the disintegration of the alginate matrix, speeding up the rate of IBU release after 150min. However, those systems containing MG nanoparticles show a more controlled release profile during the experiment, mainly in the case of beads incorporating the drug within the LDH–IBU intercalation compound. For the ALG/IBU/MG and ALG/LDH–IBU/MG systems, the maximum released amount reached values around 89% and 68%, respectively, after 7h of study. These results suggest that the hydrophobic ferromagnetic carbon/graphite can act as a protective barrier, by the water uptake results. These factors control the passage of water molecules into the beads, on condition that a delay in the kinetics of the release of the IBU into the medium. Moreover, ALG/ LDH–IBU/MG shows a slower release than ALG/IBU/MG, since the LDH-encapsulated IBU requires additional time to be released from the protective inorganic layered solid.

On the other side, Fig. 20b shows the release behavior of IBU in the case of bionanocomposites processed as films. The ALG/IBU films released around 99% of the entrapped drug and the ALG/LDH–IBU films released around 95%, at 210min and 300min of study, respectively. The ALG/LDH–IBU films reached a release

slightly slower than ALG/IBU films because of the presence of the drug intercalated in the LDH host solid as mentioned above. The influence of MG nanoparticles in the bionanocomposite behavior was observed afresh the films. The ALG/IBU/MG sample shows a slightly slower rate of release than the systems without MG, and it took longer (about 6h) to reach the total release of the drug. The ALG/LDH–IBU/MG film was again the bionanocomposite film that presented the more controlled release of the drug, reaching a release of around 81% after 8h of study. Generally, the bionanocomposites processed as films reached a higher release than those prepared as beads, because of several factors that can be related to a possible reduced degree of cross-linking in contact with the medium, facilitating the passage of water and salts into the matrices.

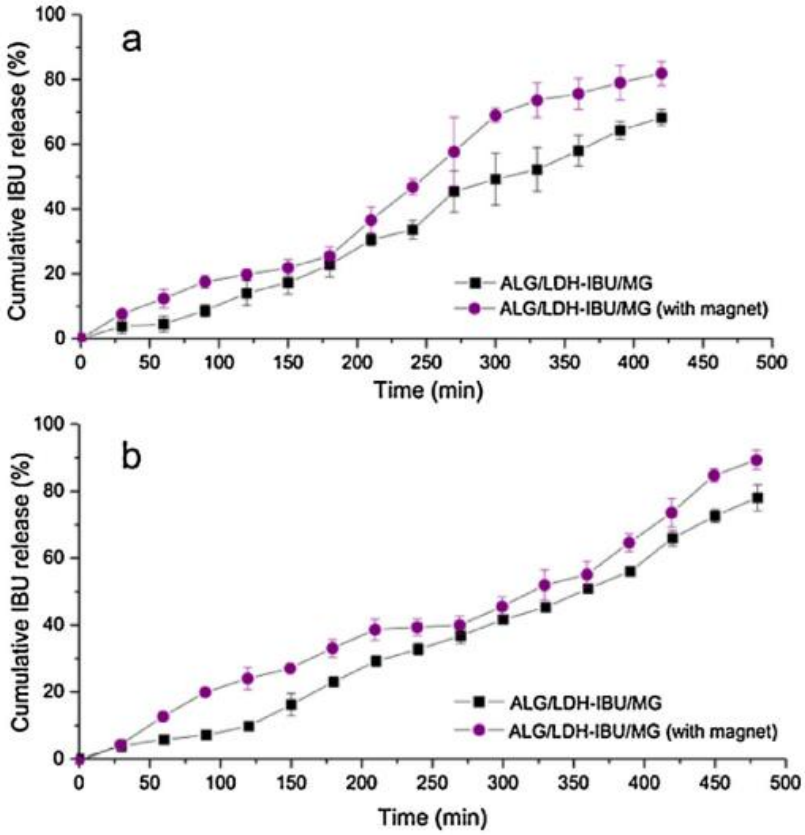

Figure 21: IBU release profile from ALG/LDH–IBU/MG bionanocomposite beads (a) and films (b) exposed or not to an external magnetic field (~ 1T), in phosphate buffer pH 7.4 at 37°C.

The ALG/LDH–IBU/MG systems presented the most progressive and controlled IBU release of all the bionanocomposites, independently of their morphology, and were chosen to study their *in vitro* drug release under a magnetic stimulation by an external magnetic field. Thus, the IBU release profiles from ALG/LDH–IBU/MG bionanocomposite beads under the application of an external magnetic field and without it are shown in Fig. 21a. It was observed a clear change in the drug release behavior when the beads were stimulated. The maximum released amount reached values of around 88% with application of the external magnetic field, i.e., almost 20% higher than the IBU released from the beads without applying the magnetic field. Similar behavior is observed for the ALG/LDH–IBU/MG films (Fig. 21b), the magnetic stimulation was responsible for the improved levels of IBU release, reaching values around 95% after 8h of study in contrast to the 81% obtained when the system was not magnetically stimulated.

Table 4: Rate constant (k) and r^2 coefficients (in parenthesis)[c] obtained based on zero-order equation from prepared formulation.

Forms	Formulation	Zero-order ($k^a \pm$ S.D.[b]) (mg h^{-1})
Beads	ALG/LDH–IBU/MG	19.49 ± 0.718 (0.922)
	ALG/LDH–IBU/MG with magnet	25.26 ± 1.146 (0.942)
Films	ALG/LDH–IBU/MG	19.51 ± 0.974 (0.946)
	ALG/LDH–IBU/MG with magnet	23.66 ± 0.769 (0.963)

[a] Rate constant.
[b] Standard deviation is the mean.
[c] Coefficient of determination (r^2).

These events could be explained by a possible alignment of the magnetic moments of the magnetic carbon/graphite nanoparticles with that of the external magnetic field, which would lead to several alterations resulting in the expansion of the bionanocomposite network and allowing the release of higher amounts of the entrapped drug to the medium, as reported in the case of hybrid magnetic hydrogels. Finally, we can appreciate that the obtained rate constant (Table 4) is higher for the magnetically stimulated bionanocomposite. Efforts are in progress to completely elucidate the effects of the external magnetic field to understand the release mechanism, however, the current results confirm that the application of the external magnetic field may modulate the levels of released IBU as it does the control of other parameters like contact time, temperature and pH, extensively reported in the literature.

4.4 FERROMAGNETIC CARBON AND MAGNETIC PARTICLE IMAGING RESULTS[9].

Magnetic particle imaging is a novel imaging modality that uses various static and oscillating magnetic fields, as well as tracer materials made from iron oxide nanoparticles to perform background-free measurements of the particles' local concentration. The method exploits the non-linear re-magnetization behavior of the particles and has the potential to surpass current methods for the detection of iron oxide in sensitivity and spatiotemporal resolution.

Nanofluids, defined as fluids containing suspended solid nanoparticles, are potential systems for utilization in biomedical applications. Magnetic Particle Imaging (MPI) uses superparamagnetic nanofluids, e.g., a colloidal suspension of iron oxide particles. Here we show a new biocompatible nanofluid based on pure and stable ferromagnetic carbon/graphite. Although this material has a small value of the coercive magnetic field, it does exhibit a true ferromagnetic behavior up to 300K. We present results obtained from numerical investigations performed to calculate the impact of a ferromagnetic magnetization on the MPI signal chain. Moreover, by modeling ferromagnetic magnetization we prove here the general suitability of ferromagnetic materials for MPI. Due to the low saturation magnetization, however, MPI for ferromagnetic carbon/graphite will be possible only in the near future when realistic concentrations of the nanofluid ferromagnetic carbon/graphite will be experimentally obtainable.

As shown before, ferromagnetic carbon/graphite can be produced by a vapor phase redox reaction in a closed nitrogen atmosphere with copper oxide (CuO). Also, our experimental report published at Nature Scientific Report confirms that ferromagnetic carbon/graphite originates from defects. They are introduced into the carbon structure by the vapor phase redox reaction. Atomic and magnetic force microscopy (AFM/MFM) can be used to study the presence of magnetic regions which are approximately 1μm. Also, the chemical route for synthesizing nanofluid ferromagnetic carbon/graphite is described in this work. The structural characterization performed by transmission electron microscopy (TEM) revealed a flake-like morphology. Relating the size of the scale in Fig. 22 (left) with the size of the particle in the nanofluid, the latter is estimated to be of the order of 10nm.

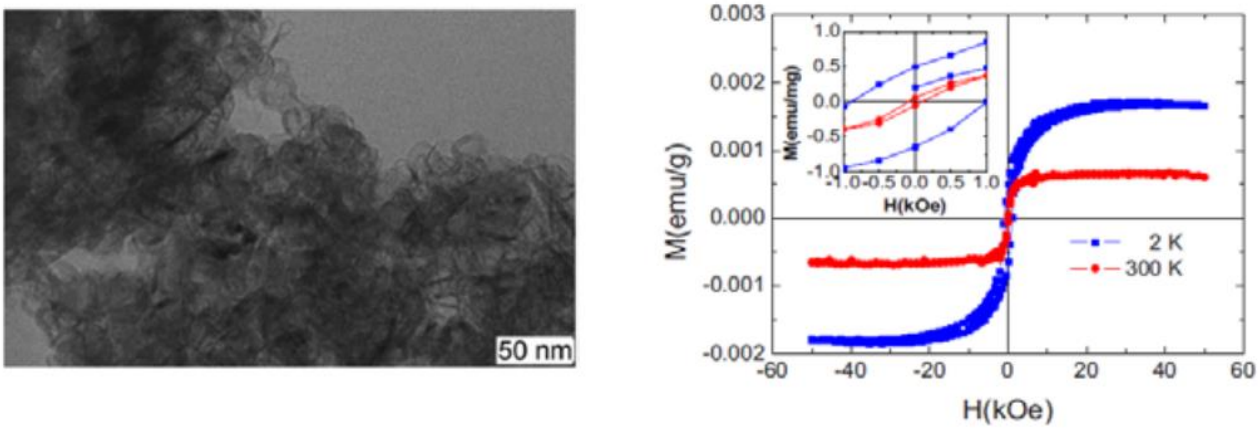

Figure 22: Left: TEM image of nanofluid ferromagnetic carbon/graphite sample showing a flake-like structure with an average size of the particle of the order of 10nm. Right: The hysteresis curves for nanofluid ferromagnetic carbon/graphite sample for two temperatures 2K and 300K showing a ferromagnetic like behavior of the sample. Inset: low-field M-H curves.

Besides, according to Fig. 22 (right), which shows M×H curves at 2K and 300K, the hysteresis does not disappear with increasing temperature and manifests itself in nonzero values of remnant magnetization and coercive magnetic field. Consequently, we can conclude that, even though the nanofluid ferromagnetic carbon/graphite has a relatively small value of coercive magnetic field (quasi-superparamagnetic state), it does exhibit a true ferromagnetic behavior up to 300K.

The stability of nanofluid ferromagnetic carbon/graphite can be verified by Zeta potential measurements of the nanoparticles under suspension. The Zeta potential indicates the level of the repulsion between particles similarly charged in dispersion. This means that the higher the Zeta potential, the more the dispersion will resist aggregation, resulting in a longer period of stability. The stability of the dispersed solution of nanofluid ferromagnetic carbon/graphite associated with its magnetic features, confirms its potential to be used in biological and medical applications, like imaging specifically MPI.

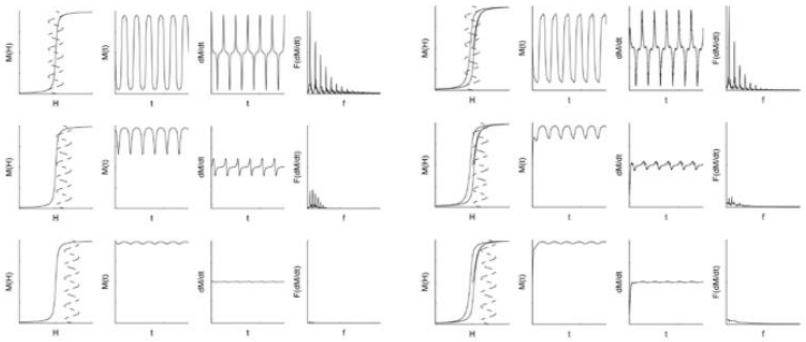

Figure 23: Comparison of MPI signals chain for three different offset fields using superparamagnetic (left) and ferromagnetic nanofluid (right).

Fig. 23 shows the MPI signal chain for superparamagnetic and ferromagnetic particles for various values of the offset field: Magnetization, induced voltage, and frequency spectrum. In both magnetization classes, higher modulation offset causes saturation of the oscillating magnetization which determines the local MPI resolution. Comparing the spectra for the same values of the offset field, differences of the amplitude of frequency peaks between the superparamagnetic and the ferromagnetic magnetization can be observed.

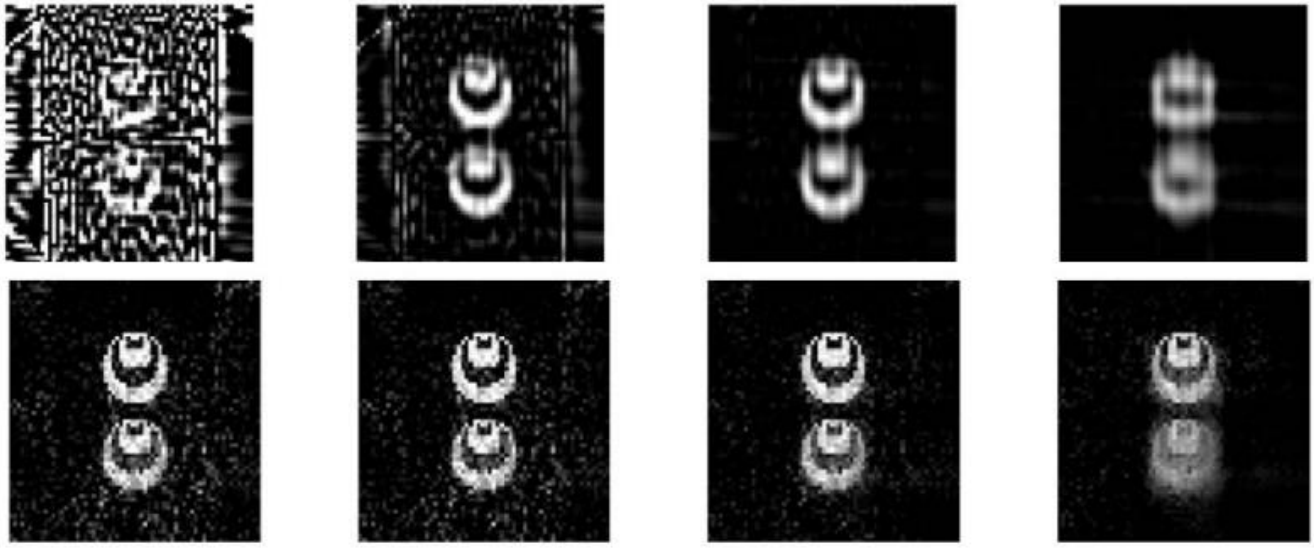

Figure 24: Results of 2D reconstruction for different regularization parameters l_k (rows) increasing from left to right and different particle models (lines): ferromagnetic model, bottom, superparamagnetic model, top. The concentration is 74.4 µmol.

Fig. 24 presents reconstruction results for both particle models. The two-dimensional object is reconstructed with a resolution of 64x64 pixels and 50 time points per sinus wave of the trajectory current. The trajectory density is κ=30. In general, image quality will increase with higher concentrations while the smoothness of the reconstructed image increases with the regularization parameter. A comparison of MPI results from superparamagnetic to those from ferromagnetic magnetization reveals the later to produce less blurred and more edged images.

4.5 MAGUS: A NEW AND PROMISING DRUG CARRIER[10].

Here, we will use all concepts and results shown in precedent sections. As we all know, potential nano-systems for uses in biological, biotechnological and medical applications are the so-called nanofluids defined as fluids containing suspended solid nanoparticles of different sizes. A most recognizable class of magnetically controllable nanofluid simultaneously exhibiting both fluid and magnetic properties is the ferrofluid. This consists of a suspended colloidal fluid of nanosized iron oxide (Fe_3O_4) particles frequently called SPIO (Superparamagnetic Iron Oxides). Instead of SPIO and aiming for applications of ferromagnetic carbon/graphite in medicine and other biotechnology related areas, we have developed – as described before **in** this work - the chemical synthesis route of nanofluid ferromagnetic carbon/graphite. We have obtained it from previously synthesized nanofluid samples by stabilizing the aqueous fluid suspension with the addition of an active cationic surfactant. The structural analysis of nanofluid ferromagnetic carbon/graphite (with an average particle size of about 10nm) confirmed its stability in aqueous solution. By measuring the magnetization as a function of temperature and applied magnetic field in both ferromagnetic carbon/graphite and nanofluid ferromagnetic carbon/graphite samples, we observed the typical ferromagnetic behavior. Instead of SPIO and aiming for applications of this material in medicine and other biotechnology related areas, we have developed the chemical synthesis route of the nanofluid material. We have obtained it from previously synthesized samples by stabilizing the aqueous fluid suspension with the addition of an active cationic surfactant. The structural analysis of the nanofluid (with

an average particle size of about 10nm) confirmed its stability in aqueous solution. By measuring the magnetization as a function of temperature and applied magnetic field in both ferromagnetic carbon/graphite and nanofluid ferromagnetic carbon/graphite samples, we observed the typical ferromagnetic behavior. The comparative study unambiguously demonstrated that, after the chemical treatment, both ferromagnetic carbon/graphite and nanofluid ferromagnetic carbon/graphite as well as all its suspensions (prepared with acetone, CTAB and water) exhibit a stable net magnetization at room temperature. Since the magnetic behavior of nanofluid ferromagnetic carbon/graphite is important for possible biological, biotechnological and medical applications, we have also studied its stability issues and the structure-sensitive magnetic properties. All samples have an average particle size of the order of 10nm. The obtained high values of the Zeta potential indicated a good stability of the dispersed solution. A rather strong reactivity between nanofluid ingredients and the cationic surfactant was evidenced by using DRIFT (*Diffuse Reflectance Infrared Fourier Transform*) spectroscopy. The measured hysteresis curves confirm a robust ferromagnetic behavior of all nanofluid ferromagnetic carbon/graphite samples at room temperature. The observed structure of sensitive temperature oscillations of the magnetization is interpreted as a strongly coherent thermomagnetic response of the nanofluid which is important for its applications in biology, biotechnology and medicine.

The first possible question arising here is if this nanofluid ferromagnetic carbon/graphite could be used as a contrast, for example, for use in the so-called MPI (Magnetic Particle Imaging) technique. We have already answered this question. The image quality using this nanofluid is comparable to or even better than for superparamagnetic nanofluids. It shows more edged and less blurred results. This may be attributed to the existence of a remnant magnetization of the ferromagnetic particles. However, due to the currently low saturation magnetization of the nanofluid ferromagnetic carbon/graphite, the generation of a strong MPI signal will only be possible in the future when high concentrations will be obtainable.

A second possible question is if ferromagnetic carbon/graphite could be used as a drug carrier. We have also answered this question. We have developed a new magnetic bio-hybrid system for potential application in drug delivery from the assembly of biopolymer alginate and ferromagnetic carbon/graphite nanoparticles. The drug Ibuprofen® (IBU) intercalated in a MgAl Layered Double Hydroxide (LDH) was chosen as a model of the Drug Delivery System (DDS) to be incorporated as a third component of the magnetic bio nanocomposite DDS. The IBU was incorporated either as the pure drug or as the LDH-IBU intercalation compound and processed as beads or films for application as drug release systems. The presence of ferromagnetic carbon/graphite nanoparticles improved the physical and mechanical properties of the resulting bio nanocomposites, decreasing the speed of drug delivery due to the protective effect as a physical barrier against water absorption into the beads. The control on the release rate was specially improved when the drug was incorporated as the LDH-IBU intercalation compound, being this fact attributed to the additional physical barrier afforded by the inorganic layered host solid. These bionanocomposite systems could be also stimulated by an external magnetic field, enhancing the levels of the released IBU, which would be advantageous to modulate the dose of the released drug when required. This new magnetic DDS could be used for immobilization of other drugs and enzymes, but also as wound dressings or as scaffolds in tissue engineering, as they could be also processed as foams, for uses in controlled drug delivery.

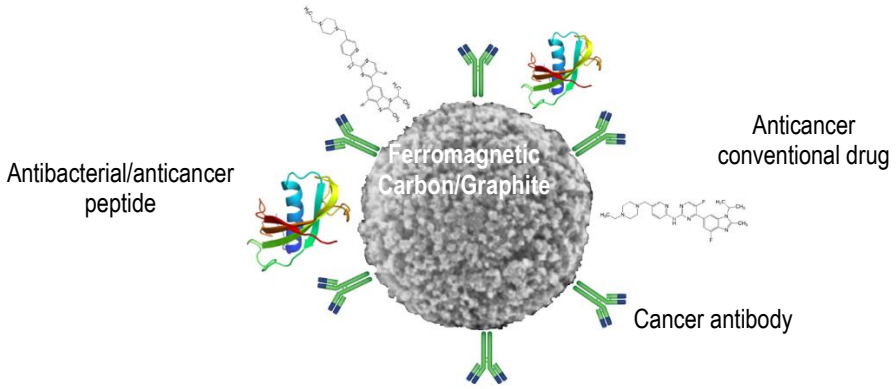

Figure 25: Sketch of carrier MAGUS®, the nanostructured drug delivery system consisting of ferromagnetic carbon/graphite functionalized with antibacterial/anticancer peptide and anticancer conventional drug for cancer treatment and the corresponding antigen-antibody interaction.

Finally, since the development of a new and efficient drug delivery system is as important as the discovery of a novel active molecule, we have built the unprecedented particle named MAGUS®, an acronym for MAgnetic Graphite Universal System. We have assembled an innovative and promising system composed of biocompatible nanostructured nanofluid ferromagnetic carbon/graphite particle coupled with different molecules simultaneously. In the world, infections contribute significantly to the emergence of cancer. Approximately twenty-three percent of cancers are a result of infections, in developing countries. Taking that into consideration, initially, we successfully assembled the system by using anticancer antibodies and two new metabolites – antibacterial and anticancer peptides - targeting to fight gastric cancer and Helicobacter pylori

infection at the same time. Before using the anticancer peptides, we have efficaciously verified the concept and well-functioning of this complex carrier by using the nanostructured biocompatible nanofluid ferromagnetic carbon/graphite functionalized with different anticancer antibodies and an anticancer drug commercially available (Fig. 25). It is important to highlight that, through the use of the interaction antigen-antibody and the possibility of magnetically directing the magnetic functionalized nanofluid ferromagnetic carbon/graphite by using an external magnetic field, we are giving our drug delivery system a double way to reach just the target, i.e. cancer, and not the healthy cells (Fig. 26). In short, we are giving specificity to the delivery system through our MAGUS® as a pioneering way to treat cancer. Something that conventional drugs and other treatments do not have at all. Now, we are testing MAGUS® to fight Alzheimer's disease following similar methodologies, following a perfect Trojan Horse method, especially for crossing the blood-brain barrier carrying the drug. We have verified that it works.

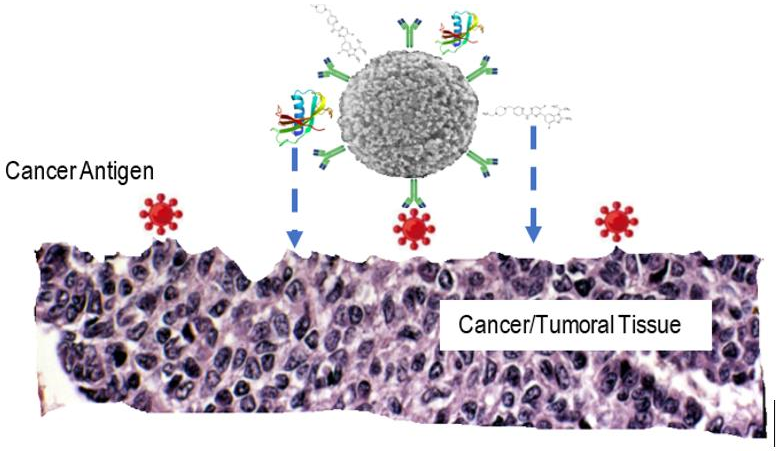

Figure 26: Sketch of MAGUS®, showing its Interactions with cancer/tumoral tissue through the action of both the antibacterial peptide and anticancer conventional drug, and the corresponding antigen-antibody interaction driven force.

4.6 MAGUS ASSOCIATED TO NUCLEAR SCIENCE AND TECHNOLOGY[11].

Developing MAGUS® associated with radioactive particles.

Besides the work carrying IBU described previously, we have also verified the concept and well-functioning of this complex carrier system by using the nanostructured biocompatible ferromagnetic carbon/graphite functionalized with different cancer antibodies focusing on the antigen-antibody interaction besides other molecules and materials. These targeting techniques include functionalizing the ferromagnetic carbon/graphite with radioactive nanoparticles like Technetium-99m, Indium-11, and Iodine-131. These radioactive nanoparticles can be produced by either synthesizing the nanoparticles directly from the radioactive materials or by irradiating non-radioactive particles with neutrons or accelerated ions. Following this principle, at present, we are functionalizing the nanostructured biocompatible ferromagnetic carbon/graphite with both Iodine-131 radioactive particles and the corresponding cancer antibody for targeting cancer cells (Fig. 27).

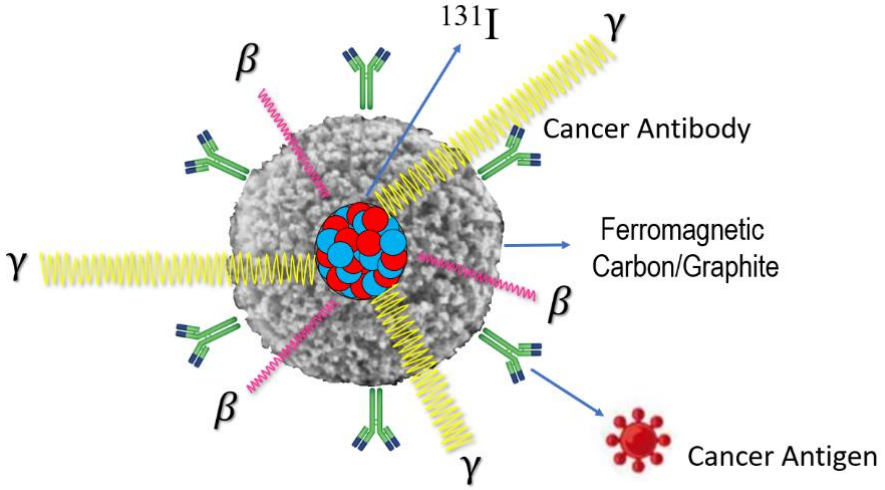

Figure 27: Sketch of MAGUS®, the nanostructured drug delivery system consisting of ferromagnetic carbon/graphite functionalized with a radioactive particle of Iodine-131 emitting gamma and beta ionizing radiation for cancer irradiation treatment and the corresponding antigen-antibody interaction.

This isotope decays with a physical half-life of 8 days to stable Xe-131. It releases radiation during the decay process by emitting beta particles and gamma. The beta particles travel about 2mm in tissue, thereby ensuring local treatment of the cancer tumor by causing mutation and death in cells that it penetrates. For this reason, high doses of the isotope are sometimes less dangerous than low doses since they tend to kill normal tissues that would otherwise become cancerous because of the radiation. Thus, Iodine-131 is increasingly less employed in small

doses in medical use but increasingly is used only in large and maximal treatment doses, as a way of killing targeted cancer tissues. Iodine-131 is given for therapeutic use since about 10% of its energy and radiation dose is via gamma radiation while the other 90% is the beta radiation mentioned before. Again, by the interaction antibody-antigen, we are giving to our drug delivery system a double way to reach just the target, i.e. the cancer, and not the healthy cells (Fig. 28).

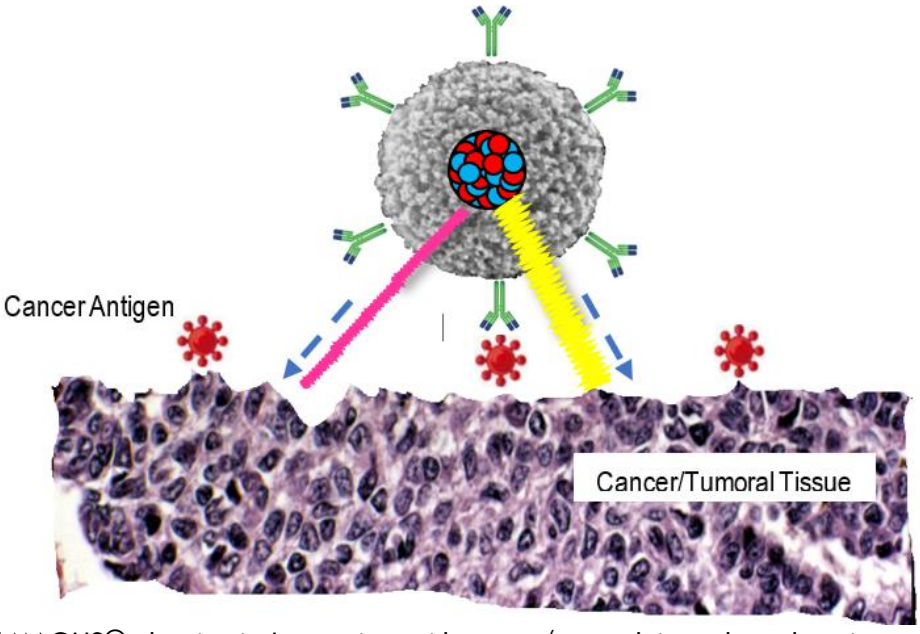

Figure 28: Sketch of MAGUS®, showing its Interactions with cancer/tumoral tissue through antigen-antibody driven force and the radiation from Iodine-131 (beta and gamma).

Developing MAGUS® associated with boron neutron capture therapy (BNCT) technique.

Another promising application we are at present working on is based on MAGUS® associated with Boron Neutron Capture Therapy (BNCT). This technique uses neutrons as the external source and is frequently used to treat specific tumors that are radio resistant or very difficult to kill using conventional radiation therapy. It can be employed as a standalone radiation therapy or in combination with conventional radiotherapy methods. Some examples where it has proven to be very powerful and effective are in treating salivary gland tumors and certain forms of cancer, such as adenoid cystic carcinoma, inoperable/ recurrent salivary gland malignancies resistant to standard low-LET radiotherapies and glioblastoma (high-grade glioma, GBM), a prevalent and aggressive brain tumor. The BNCT uses Boron-containing drugs to deliver a natural isotope of the Boron-10 to tumors and while it is confined to tumors, as radionuclides tend to accumulate at the sites of tissue damage, a subsequent bombardment with neutrons provides an isotope of Lithium-7 and an alpha particle with a short range of action. It means that the alpha particle deploys an amount of energy that is delivered in a high linear energy transfer (LET) due to its nature. In that case, their high energy will be delivered along their very brief pathway (types of radiation. Since surprisingly they do not damage equally all cells, there are cases in which they can be more damaging to cancerous cells than to healthy cells surrounding cancer. Therefore, for the same amount of radiation, a lethal dose can be delivered to the cancer cells, while a sub-lethal dose is delivered to the healthy tissue reducing the chances of cell damage or death. Used thoroughly, this different impact can be an advantage in certain treatments. In general, neutron therapy shows high efficiency in the treatment of recurrent voluminous tumors of complex localization. The approach we are working on for the BNCT application is based on functionalizing the nanostructured biocompatible ferromagnetic carbon/graphite with Boron-10 (instead of Iodine-131) with the antibodies mentioned before. Then, we apply an external magnetic field to redirect the Boron-10 and employ the fast neutron dose more efficiently at the tumor, making it necessary for a lower dose to accomplish the same results. This is especially important for BNCT because fast neutron therapy is limited by high toxicity. That is why we are providing once again to the system a double way to exclusively reach the target and not the healthy cells around increasing its efficiency and performance. It is important to highlight that, by using both the interaction antigen-antibody and the guidance through an external magnetic field, we are affording our drug delivery system a double way to reach and act only the target, i.e., cancer and not the healthy cells around. Moreover, the target- specificity achieved by our delivery system MAGUS® comes from years of research of our group and represents a pioneering and effective way to treat cancer.

5. Summary and Conclusions

Over the last decades, the survey for macroscopic magnetic ordering phenomena in organic materials was one of the most exciting and interesting subjects in both Physics and Chemistry. Achieving striking properties in macroscopic stable room-temperature bulk ferromagnetic carbon/graphite is now opening an enormous number of novel applications. The possibility of nanostructured a magnetic material of this type has increasingly attracted the interest of the scientific community, not only because of their physical and chemical properties but mainly because of their potential

applications in advanced engineering and high-tech devices. The experimental confirmation that magnetism in ferromagnetic carbon/graphite originates from defects in the structure (and not from ferromagnetic impurities of any type) allowed us to consider its potential use also in medicine, biology, and biotechnology. The nanostructured ferromagnetic carbon/graphite we synthesized for the first time in 2004 by following an unprecedentedly simple and cheap chemical process, appears as a very promising way to achieve countless valuable goals mainly in medicine. It has shown itself to be superior in many aspects to the available solutions for some aggressive and prevalent types of tumors or even for recurrent voluminous tumors of complex localization due to its combined physical properties coupled with biological and physical functionalization. By using both the interaction antigen-antibody and the guidance through an external magnetic field, we are affording our drug delivery system (using or not radioactive materials) a double way to reach and act only on the target, i.e., cancer, and not the healthy cells around. In short, we are giving specificity to the delivery system through our MAGUS® as a pioneering way to treat cancer. Something that conventional drugs and other treatments do not have at all.

In summary, in this review, exclusively about our own work, we described the obtention and main properties of carbon-based nanostructured magnetic material and how it is starting to be one of the promising materials with novel applications in medicine.

We hope that this work will encourage and motivate other scientists to join us using MAGUS or even the magnetic bio-hybrid matrices in oncology aiming to detect and fight cancer and tumors/neoplasms.

Acknowledgements: We are thankful Dr J. R. Soares-Salgado for technical reading of the manuscript. We are also deeply thankful to all my colleagues, partners, collaborators, students, and research agencies who contributed to this work for almost two and half decades. We also thank Brazilian Army, in special the Military Institute of Engineering (IME) and funding agencies FAPESP, CAPES and FINEP for valuable financial support.

Conflict of Interest: We declare that do not exist any financial or even conflicts of interest.

References

1. Galdino J. F.; Collection of opinion articles on strategic studies in defense and security. ISBN 978-65- 87080-44-4; JC Sanches, FM Araujo-Moreira. 2023; 155.
2. Cancer statistics, 2024 - PubMed (nih.gov) CA Cancer J Clin; doi: 10.3322/caac.21820 (2024).
3. Mombrú A.W., Pardo H., Faccio R., De Lima O.F., Leite E.R., Zanelatto G., Lanfredi A.J.C., Cardoso C.A., and Araújo-Moreira F.M.; Phys. Rev. B (Rapid Comm.) (2005); 71:100404(R); T. L. Makarova, Semiconductors 38, 615, (2004); P. Turek, K. Nozawa, D. Shiomi, K. Awaga, T. Inabe, Y. Maruyama, and M. Kinoshita, Chem. Phys. Lett. 180, 327 (1991); P. M. Allemand, K. C. Khemani, A. Koch, F. Wudl, K. Holczer, S. Donovan, G. Gruner, and J. D. Thomson, Science 253, 301 (1991d. 4T. L. Makarova, B. Sundqvist, R. Höhne, P. Esquinazi, Y. Kopelevichk, P. Scharff, V. A. Davydov, L. S. Kashevarova, and A. V. Rakhmanina, Nature sLondond 413, 716 (2001); R. A. Wood, M. H. Lewis, M. R. Lees, S. M. Bennington, M. G. Cain, and N. Kitamura, J. Phys.: Condens. Matter 14, L385 (2002); Y. Kopelevich, P. Esquinazi, J. H. S. Torres, and S. Moehlecke, J. Low Temp. Phys. 119, 691 (2000); P. Esquinazi, A. Setzer, R. Höhne, C. Semmelhack, Y. Kopelevich, D. Spemann, T. Butz, B. Kohlstrunk, and M. Losche, Phys. Rev. B 66, 024429 (2002); J. M. D. Coey, M. Venkatesan, C. B. Fitzgerald, A. P. Douvalis, and I. S. Sanders, Nature, Londond 420, 156 (2002); P. Esquinazi, D. Spemann, R. Höhne, A. Setzer, K. H. Han, and T. Butz, Phys. Rev. Lett. 91, 227201)2003); A. V. Rode, E. G. Gamaly, A. G. Christy, J. G. Fitz Gerald, S. T. Hyde, R. G. Elliman, B. Luther-Davies, A. I. Veinger, J. Androulakis, and J. Giapintzakis, Phys. Rev. B 70, 054407 (2004).
4. Pardo H., Faccio R., De Lima O.F.; and Araújo-Moreira F.M.; Carbon. 44:565–569 (2006).
5. Freitas J.C., Scopel W.L., Paz W.S., Bernardes L.V., Cunha-Filho F.E., Speglich C., Araújo-Moreira F.M., Pelc D., Cvitanić T., Požek M. Sci Rep. 5:14761 (2015). doi: 10.1038/srep14761. PMID: 26434597; PMCID: PMC4593005.
6. Souza N.S., Sergeenkov S., Speglich C., Rivera V.A.G., Cardoso C.A., Pardo H., Mombrú A.W., Rodrigues A.D., De Lima O.F., Araújo-Moreira F.M.; Appl. Phys. Lett.; 95:23; 233120 (2009).
7. Souza N.S., Sergeenkov S., Rodrigues A.D., Cardoso C.A., Pardo H., Faccio R., Mombrú A.W., Galzerani J.C., De Lima O.F., and Araujo-Moreira F.M.; J. of Nanofluids; 1:143–147 (2012).
8. Ribeiro L.N., Alcântara A.C., Darder M., Aranda P., Herrmann P.S. Jr, Araújo-Moreira F.M., García-Hernández M., Ruiz-Hitzky E.; Int J Pharm. 477(1-2):553-63 (2014). doi: 10.1016/j.ijpharm.2014.10.033. Epub 2014 Oct 16. PMID: 25455784.
9. Thorsten M. Buzug, Jörn Borgert, *Magnetic particle imaging: a novel SPIO nanoparticle imaging technique*, SPPHY 140, pp 15-20, Springer Science & Business Media, (2012).
10. Fernando M. Araujo-Moreira and Nadja F.G. Serrano; Crimson Publishers; Research & Development in Material Science **17**, 2, 1944 – 1946 (2022).
11. E.B. Simão-Silva, N.F.G. Serrano, M.P.C. de Medeiros, A.J. Boareto-Mendes, J.F. Galdino, and F.M. Araujo-Moreira; *Nuclear science and magnetic carbon: a promising way from a chemical method to detect and fight cancer and tumors/neoplasms*; Ann Adv Chem. 2023; 7: 047-050 (2023). doi: 10.29328/journal.aac.1001042.

